Analytical Kirchhoff Solutions (AKS) and Numerical Kirchhoff Approach (NKA) for First-Principle Calculations of Coherent Waves and Incoherent Waves at P Band and L Band in Signals of Opportunity (SoOp)

Bowen Ren, Jiyue Zhu, Leung Tsang[*], and Haokui Xu

Abstract—In this paper, we derived Analytical Kirchhoff Solutions (AKS) for bistatic scattering near the specular directions at P band and L band for applications in Signals of Opportunity (SoOp). The land surface profiles are divided into three scales: microwave roughness f_1, fine scale topography f_2, and coarse scale 30-meter DEM f_3. The microwave roughness and the fine scale topography are treated as random rough surfaces, while the coarse scale topography from DEM data are treated as deterministic planar patches. The salient features of the AKS model are (i) analytical expressions are obtained for both coherent waves and incoherent waves, (ii) Monte Carlo simulations are not required making the AKS computationally efficient, (iii) the analytical solutions are expressed in terms of the spectrum, so that the dividing line between microwave roughness and fine scale topography is not required, and the rough surface spectrum derived from lidar elevation measurements can be incorporated directly. The results of the three approaches, AKS, the Numerical Kirchhoff Approach (NKA) and the Fine Scale Partial Coherent Patch (FPCP) model, are indistinguishable for both the coherent waves and the incoherent waves. The agreements validate the AKS and FPCP approaches as NKA is a brute force accurate method based on Kirchhoff integral using 2 cm discretization and high-performance computers. Results show that the f_2 profiles of fine scale topography have significant effects. The results of three Kirchhoff approaches fall in-between the results of the two versions of Geometric Optics (GO) approximations to the Kirchhoff integral [1, 2]. The two GO versions are with and without attenuation due to microwave roughness. The GO with microwave attenuation is also known as the "Improved Geometric Optics Model (IGOM)". Numerical results of coherent waves and incoherent waves are illustrated for remote sensing of snow and soil moisture at P band and L band. For P band, the histograms of the phase are shown. Results of the coherent waves are dependent on the sizes of the area as well as topographical elevations and slopes. AKS results are used to illustrate the coherent waves at P band on area sizes up to 1.5 km using 30-meter DEM topography elevations and derived slopes at Sanford, Brazos Peak, and Lobato Tank, Colorado, USA. For L band, the AKS results of Cross-Track are in good agreement with CYGNSS data over San Luis Valley, USA. In comparing CPU, it takes merely 25 seconds on a single CPU core for AKS to compute for a 15 km by 15 km DDM pixel which has 250000 DEM 30-meter patches. The CPU for AKS is slightly more than the 20 seconds required for GO.

1. INTRODUCTION

In P band and L band Signals of Opportunities (SoOp), the transmitters on existing satellites are utilized. Satellites with receivers are launched to measure the reflected signals. Global Navigation Satellite System Reflectometry (GNSS-R) is an application of SoOp at L band. The operating GNSS-R missions includes the Techdemosat-1 (TDS-1) [3] launched by UK in 2014, the Cyclone Global

Navigation Satellite System (CYGNSS) [4] launched by NASA in 2016, and Bufeng launched by China in 2019. The GNSS-R data are collected in the form of Delay Doppler Maps (DDMs), which have been applied to the retrieval of ocean wind speed [5], sea ice thickness [6], and monitoring the wetland changes [7]. Researchers have shown the potential of soil moisture retrieval by the GNSS-R data [8–10]. Recently there are also interests in using the phase of the P band signals of opportunities. In Reference [11], it is proposed to infer snow water equivalent using the phase of the reflected waves.

There are major differences between the usual rough surface bistatic scattering formula and the reflected signals in SoOp. In the usual rough surface bistatic scattering, the formula is an extension of radar backscattering [12]. In radar rough surface backscattering from soil surfaces, contributions to σ_0 come from the microwave roughness which have large slopes. In extension to bistatic scattering, the formula is merely the radar backscattering with the scattered direction changed to that of the bistatic direction and thus only the contributions from microwave roughness are included. However, in reflection from signals of opportunities including GNSS-R, the scattered direction is in the vicinity of the specular direction within a few degrees. The first difference of this close to specular scattering is that the bistatic scattering has both the coherent waves and the incoherent waves. Thus, both the coherent waves and incoherent waves need to be included in the σ_0 [12]. The second difference is that even if the coherent waves are ignored, the remaining bistatic incoherent waves are strongly dependent on topographical elevations and slopes which can affect the σ_0 by many decibels. Without including the effects of topography, the physical models of rough surface bistatic scattering of the incoherent waves are not valid. For L band microwave remote sensing of soil moisture, the models of SMAP (soil moisture active and passive) and NISAR (NASA-ISRO SAR) include primarily the effects of microwave roughness with topography playing a lesser role. On the other hand, the models of CYGNSS have to be different from that of SMAP and NISAR. The CYGNSS models need to include the effects of land topography as topography plays a major role.

In the past, there are three physical models. One is the extension of the radar backscattering of microwave roughness to the bistatic direction as described earlier. The second model is the coherent model which uses the image theorem of a point source to obtain the reflected signal that captures the Fresnel zone effects. The results are multiplied by an attenuation factor $\exp(-4k^2h_1^2\cos^2\theta_i)$, where h_1 is the root mean square (rms) height of microwave roughness, k is the wave number and θ_i is the incident angle. The attenuation factor is quite significant. For microwave roughness of $h_1 = 3\,\mathrm{cm}$, $\theta_i = 40°$, the attenuation factor is $-10\,\mathrm{dB}$. The third model is the incoherent model which is based on the assumption that because of the topographical large elevation changes in land surfaces, the received signal is incoherent. The incoherent models are based on Geometric Optics (GO) model. The GO model is also an approximation of Kirchhoff integral using the method of stationary phase. In GO model, the scattered intensity is proportional to probability density function $p_{\mathrm{pdf}}(p,q)$ where p and q are the slopes in the horizontal x and y directions, respectively [12]. The choice of pdf is Gaussian, so that $p_{\mathrm{pdf}}(p,q) = \exp[-(p^2+q^2)/(2s^2)]/(2\pi s^2)$, where s is the rms slope and a small number is usually used. It was first used in GNSS-R for ocean reflection [13] by truncating the ocean spectrum to eliminate the small roughness so as to derive the pdf of slopes. For GNSS-R land applications, it was also used by [1] and [2]. However, a second version of geometric optics in ocean problem was proposed [14] in which the attenuation factor $\exp(-4k^2h_1^2\cos^2\theta_i)$ is attached to account for the effects of microwave small roughness. It is labelled as the "Improved Geometric Optics Model (IGOM)", which is GO-Att (Geometric Optics with Attenuation). The GO model was applied to land surfaces [1]. The "Improved Geometric Optics model" was also applied recently to land surface [15].

In applying to land, the surface heights are composed of a summation of three kinds of roughness/topography (Fig. 1):

$$z = f_1(x,y) + f_2(x,y) + f_3(x,y) \tag{1}$$

where $f_1(x,y)$ is the microwave roughness with rms height of 6 cm or less, and f_2 and f_3 are the topography. In the CYGNSS project, extensive measurements are taken to measure the rms heights and correlation lengths of the microwave roughness at San Luis Valley [16]. The topography $f_3(x,y)$ is the coarse scale topography as given by DEM. It is labelled as "coarse" because the DEM is of horizontal resolution of 30 m. A linear interpolation is used to obtain $f_3(x,y)$, so that $f_3(x,y)$ corresponds to tilted planar patches with 30 meter scale. The $f_2(x,y)$ is labelled as "fine scale topography" that is in-between the coarse topography and the microwave roughness. The fine scale topography $f_2(x,y)$ will have rms
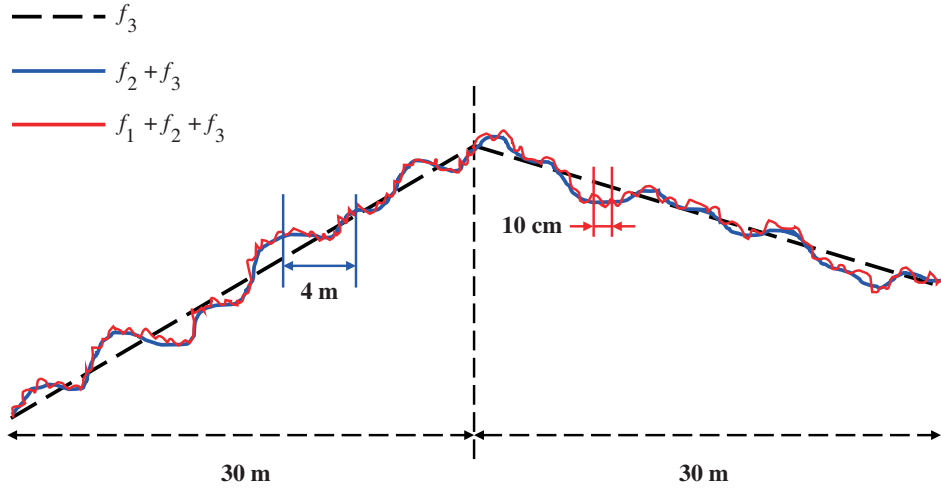
Figure 1. Profile of $f = f_1 + f_2 + f_3$. f_1: microwave roughness, f_2: fine scale topography, f_3: planar from DEM. f_1 and f_2 are random, f_3 is deterministic.

height of 5 cm and above and horizontal correlations of 0.5 m to 10 m. Recently, lidar measurements have been taken [17]. For future works, such fine-scale measurements and the derived spectrum will be used to infer $f_2(x, y)$.

In the improved geometrical optics model [14], the factor $p_2(-k_{dx}/k_{dz} - p_3, -k_{dy}/k_{dz} - q_3)$ is used where the arguments p_3 and q_3 are the slopes of f_3 while the function p_2 is the pdf of slopes of $f_2(x, y)$. The parameter $s = 0.75°$ is used in the slopes pdf of Gaussian distributions. In the argument, k_{dx}/k_{dz} and k_{dy}/k_{dz} are used to denote the deviations from the specular direction when the f_3 patches are at a distance from the specular point.

Other models include the Soil And VEgetation Reflection Simulator (SAVERS) model [18]. In the SAVERS model, the $f_2(x, y)$ is not used. Instead extensive averaging are taken over the slopes of the planar patches of $f_3(x, y)$ to obtain the pdf of slopes. In SAVERS, the attenuation factor $\exp\left(-4k^2 h_1^2 \cos^2 \theta_i\right)$ is also used.

In our approach, we have used the vector Kirchhoff based approach. Although the vector Kirchhoff approach is not valid for radar backscattering particularly for the VV polarization, it is quite accurate in the vicinity of the specular direction as shown by numerical solutions of Maxwell equations. In Table 1, we summarize our three approaches. The first approach, what we initially used, is a numerical Kirchhoff approach [19]. We used patch size of 2 cm in the numerical discretization of calculating the Kirchhoff integral. The surface is characterized by the height function $f = f_1 + f_2 + f_3$. Because of fluctuations due to f_1 and f_2, Monte Carlo simulations are performed and averages are taken over realizations over f_1 and f_2. The results are treated as having benchmark accuracy as no approximations are used aside from the Kirchhoff integral. Intensive CPU are required with high performance computation. In the second approach, Fine Scale Partial Coherent Patch (FPCP) model [20, 21], we perform the Kirchhoff integral with patch sizes $L = 1$ m or 2 m. The patches are planar patches with p_m and q_m being the slopes of the mth patch of $f_2 + f_3$. Superimposed on the mth patch is the microwave roughness $f_1(x, y)$. Analytic rough surface scattering theory is applied to microwave roughness $f_1(x, y)$ with coherent and incoherent waves. In summing over the 1-meter or 2-meter patches, field summations are carried out for the coherent waves and intensity summations for incoherent waves. Because of random fluctuations of f_2, Monte Carlo simulations are performed over realizations of $f_2(x, y)$.

In this paper we present our new third approach, the Analytical Kirchhoff Solution (AKS). In this approach we use $f_{12} = f_1 + f_2$ combined. The roughness f_{12} is superimposed on the f_3 planar patches of DEM. Then rough surface scattering theory is applied to $f_{12}(x, y)$ with analytical solutions derived for the coherent waves and incoherent waves. The salient features of the AKS model are (i) analytical expressions are obtained for both coherent and incoherent waves, (ii) Monte Carlo simulations are not required making the AKS computationally efficient, (iii) the analytical solutions are expressed in terms

Table 1. Summary of three approaches.

	Numerical Kirchhoff Approach (NKA) Gu et al., 2019 [19]	Fine Scale Partial Coherent Patch (FPCP) model Xu et al., 2021 [21]	Analytical Kirchhoff Solution (AKS) this paper
Discretization	2 cm	1 m to 2 m	30-meter DEM patch
Monte Carlo simulations	Monte Carlo speckle fluctuations	Monte Carlo speckle fluctuations	Analytical No Monte Carlo No fluctuations
CPU time for one DDM of 15 km (details in Table 8)	Intensive	Moderate	Fast
Validation	Accurate benchmark based on brute force calculations	Validated by NKA	Validated by NKA
DEM coarse f_3	planar, deterministic	planar, deterministic	planar, deterministic
Fine scale f_2: random	Monte Carlo average	Monte Carlo average	Analytical average
Microwave f_1: random	Monte Carlo average	Analytical average	Analytical average
Combining roughness	$f = f_1 + f_2 + f_3$ combined dividing line not needed	f_1 and f_2 separate dividing line needed	$f_{12} = f_1 + f_2$ combined dividing line not needed
Spectrum $W(k)$	Can directly use $W(k)$	Need to split $W(k)$ into f_1 and f_2	Can directly use $W(k)$
Histogram statistics of amplitude and phase	Yes	Yes	No

of the spectrum so that the dividing line between microwave roughness and the fine scale topography is not required, and the rough surface spectrum derived from lidar elevation measurements [17] can be incorporated directly. The results of the three approaches AKS, Numerical Kirchhoff Approach (NKA) and the Fine Scale Partial Coherent Patch (FPCP) model are indistinguishable for both the coherent waves and the incoherent waves. The agreements validate the AKS and FPCP approaches as NKA is a brute force accurate method using 2 cm discretization and high-performance computers. In Table 1, we compare the three approaches. Since the three approaches give indistinguishable results, we shall label the results as Kirchhoff approach. The numerical results of the Kirchhoff approach are compared with that of GO and GO-Att (IGOM). Numerical results of coherent waves and incoherent waves are illustrated for L band and P band. AKS results are used to illustrate the coherent waves at P band on area sizes up to 1.5 km using 30-meter DEM topography elevations and derived slopes at Sanford, Brazos Peak, and Lobato Tank, Colorado, USA. For L band, the AKS results of Cross-Track are in good agreement with CYGNSS data over San Luis Valley, USA.

The paper is organized as following. In Section 2, we give the geometric descriptions of the configurations of transmitter and receiver, and topography and rough surface of land surfaces. In Section 3, we derive Analytical Kirchhoff Solutions (AKS) for coherent and incoherent waves for a single $f_3(x, y)$ DEM patch. In Section 4, we give the results of multiple DEM 30 m planar patches with summation of coherent fields and summation of incoherent intensities. In Section 5, we review and summarize the formulas of Numerical Kirchhoff Approach (NKA) and Fine Scale Partial Coherent Patch (FPCP) model. In Section 6, we give formulas of GO and GO-Att. In Section 7, we review and summarize equations for Track Results. In Section 8, numerical results are illustrated for L band. In Section 9, results are illustrated for P band. The emphasis of P band is on the bistatic scattering coefficients of the coherent waves with variations of elevations, topographical slopes and area sizes. In Section 10, we have CPU comparisons of the incoherent waves of NKA, AKS, and GO for a DDM pixel of size 15 km × 15 km. The CPU for AKS is only 25 seconds. Section 11 is the conclusion.

2. GEOMETRIC DESCRIPTIONS OF GNSS-R: TOPOGRAPHY AND ROUGH SURFACE

We consider the surface height $f(x, y)$ as composed of a summation of three kinds of roughness/topography (Fig. 1):

$$f(x, y) = f_1(x, y) + f_2(x, y) + f_3(x, y) \qquad (2)$$

We shall define:

$$f_{12}(x, y) = f_1(x, y) + f_2(x, y) \qquad (3)$$

where $f_1(x, y)$ is the microwave roughness with rms height of 0.25 wavelength or less. $f_3(x, y)$ is the DEM topography at 30-meter scale. The intermediate scale $f_2(x, y)$ is labelled as fine scale topography between microwave roughness and DEM topography. Previously, profiles of $f_2(x, y)$ are largely unknown. However, recent lidar measurements confirm the existence of non-zero $f_2(x, y)$. We shall assume $f_1(x, y)$ and $f_2(x, y)$ as stochastic Gaussian process that is statistical homogeneous. The $f_3(x, y)$, derived from DEM, is deterministic and will be assumed to be consisting of planar patches of 30 meters with slopes p_3 and q_3 in the x and y directions respectively. This means that the second order derivatives of $f_3(x, y)$ are equal to zero. Thus, the geometry consists of DEM 30-meter planar patches with stochastic roughness $f_1(x, y)$ and $f_2(x, y)$ superimposed on them.

The stochastic descriptions of $f_1(x, y)$, $f_2(x, y)$, and $f_{12}(x, y)$ are shown in Table 2. For real life profiles, it can be difficult to form a dividing line between f_1 and f_2. Thus, the last column $f_{12}(x, y)$ is a combination of microwave roughness and fine scale topography without a dividing line. In Table 2, we also list the correlation functions and the spectral densities. The combined case of $f_{12}(x, y)$ is the general case with correlation function $h^2 C(x, y)$ and spectral density of $W(k_x, k_y)$. The decompositions of $f_{12}(x, y)$ separately into $f_1(x, y)$ and $f_2(x, y)$ are special cases of $f_{12}(x, y)$.

Table 2. Descriptions of $f_1(x, y)$ and $f_2(x, y)$.

Scales	Microwave Roughness $f_1(x, y)$	Fine Scale Topography $f_2(x, y)$	Combined f_1 and f_2 without dividing line $f_{12}(x, y)$
Correlation Function	$h_1^2 C_1(x, y)$	$h_2^2 C_2(x, y)$	$h^2 C(x, y)$
Spectrum	$W_1(k_x, k_y)$	$W_2(k_x, k_y)$	$W(k_x, k_y)$

Since $f_{12}(x, y)$ is statistical homogeneous, the correlation function is:

$$h^2 C(x, y) = \left\langle f_{12}\left(x', y'\right) f_{12}\left(x' + x, y' + y\right) \right\rangle = \iint\limits_{-\infty}^{+\infty} dk_x dk_y W\left(k_x, k_y\right) \exp\left(i k_x x + i k_y y\right) \qquad (4)$$

with $C(0, 0) = 1$. Then we have:

$$h^2 = \iint\limits_{-\infty}^{+\infty} dk_x dk_y W\left(k_x, k_y\right) \qquad (5)$$

For the case of isotropic rough surface:

$$h^2 C(x, y) = h^2 C(\rho) = 2\pi \int\limits_0^{+\infty} dk_\rho k_\rho W\left(k_\rho\right) J_0\left(k_\rho \rho\right) \qquad (6)$$

where J_0 is the Bessel function of zeroth order. Let the GNSS-R transmitter and receiver be located in the xz plane, as shown in Fig. 2. Note that the transmitter is located at:

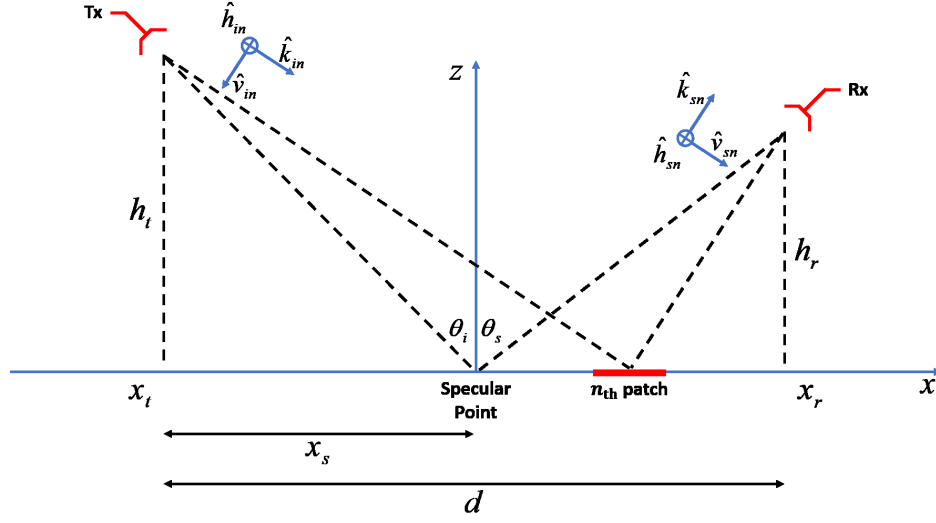$$\text{Tx} = (x_t, 0, h_t) \qquad (7)$$

Figure 2. Specifications of transmitter and receiver, and definitions of patches and wave vectors.

Let the receiver be located at:
$$\text{Rx} = (x_r, 0, h_r) \tag{8}$$

Since x_t is negative, let
$$x_s = -x_t \tag{9}$$

Then
$$x_r + x_s = d$$
$$x_s = -x_t = \frac{dh_t}{h_r + h_t} \tag{10}$$
$$x_r = \frac{dh_r}{h_r + h_t}$$

In GNSS-R applications, the receivers are in the specular directions, which means that d can be expressed in terms of the incident angle θ_i:
$$\frac{d}{h_r + h_t} = \tan \theta_i = \tan \theta_s \tag{11}$$

Thus, we have:
$$x_s = -x_t = h_t \tan \theta_i$$
$$x_r = h_r \tan \theta_s \tag{12}$$

3. ANALYTICAL KIRCHHOFF SOLUTIONS (AKS) COHERENT AND INCOHERENT FIELDS FOR A SINGLE DEM PATCH

We first consider a single 30 m planar patch as given by $f_3(x, y)$. The single patch is labeled as "nth patch". The stochastic roughness and fine scale topography $f_{12}(x, y)$ is superimposed on the planar patch (Fig. 1). Let the center of the patch be at:
$$\bar{r}_n = x_n \hat{x} + y_n \hat{y} + z_n \hat{z} \tag{13}$$
in which $z_n = f_3(x_n, y_n)$. The slopes of the $f_3(x, y)$ planar patch are:
$$\frac{\partial f_3}{\partial x}(x_n, y_n) = p_{3n}$$
$$\frac{\partial f_3}{\partial y}(x_n, y_n) = q_{3n} \tag{14}$$

For the nth planar patch, $f_3(x, y)$ is a linear function:

$$f_3(x, y) = z_n + p_{3n}(x - x_n) + q_{3n}(y - y_n) \tag{15}$$

The distances between the patch center and the transmitter and the receiver are respectively R_{nt} and R_{nr}:

$$R_{nt} = \sqrt{(x_n - x_t)^2 + y_n^2 + (z_n - h_t)^2}$$
$$R_{nr} = \sqrt{(x_n - x_r)^2 + y_n^2 + (z_n - h_r)^2} \tag{16}$$

In applying analytical Kirchhoff, far field approximations are assumed for the discretization into patches of sizes L. This means that the incident field to the nth patch is approximated by a plane wave of direction $\hat{k}_{in}$. From the patch to the receiver, the received field is a plane wave in direction $\hat{k}_{sn}$. The far field approximation means:

$$R_{nt}, R_{nr} \gg \frac{L^2}{\lambda}$$
$$L \ll \sqrt{\lambda R_{nt}}, \sqrt{\lambda R_{nt}} \tag{17}$$

In GNSS-R, the elevation of the transmitter is much larger than that of the receiver, which is $R_r = 500\,\text{km}$. For P band, we have $freq = 370\,\text{MHz}$, $\lambda = 0.81\,\text{m}$. For L band, $freq = 1.575\,\text{GHz}$, $\lambda = 0.19\,\text{m}$. Thus,

$$L \ll 308\,\text{m}, \quad \text{L band}$$
$$L \ll 636\,\text{m}, \quad \text{P band} \tag{18}$$

is required over the domain of integration. If the discretizations are less than that requirement, then the variations of the scattered field direction and the variations of the phase factor need to be variables over the domain the integration.

Because the patch size for DEM is only $L = 30$ meters Fraunhofer far field assumption holds for both incidence wave and scattered wave. The definitions of the wave vectors are illustrated in Fig. 2. The wave vector of the incidence plane wave is:

$$\hat{k}_{in} = k_{inx}\hat{x} + k_{iny}\hat{y} - k_{inz}\hat{z}$$
$$k_{inx} = \frac{k(x_n - x_t)}{R_{nt}}$$
$$k_{iny} = \frac{ky_n}{R_{nt}}$$
$$k_{inz} = \frac{k(h_t - z_n)}{R_{nt}} \tag{19}$$

The incident angle θ_{in} on the patch is:

$$\cos(\theta_{in}) = \frac{k_{inz}}{k} \tag{20}$$

The horizontal and vertical polarizations are:

$$\hat{h}_{in} = \frac{\hat{z} \times \hat{k}_{in}}{\left| \hat{z} \times \hat{k}_{in} \right|}$$
$$\hat{v}_{in} = \hat{h}_{in} \times \hat{k}_{in} \tag{21}$$

Let the x', y' coordinates be relative to the patch center. Then:

$$x' = (x - x_n); \quad y' = (y - y_n) \tag{22}$$

Let $\bar{r}'$ be the position on the rough surface relative to the patch center. The vertical displacement of the rough surface relative to the patch center is:

$$z' = p_{3n}x' + q_{3n}y' + f_{12}(x', y') \tag{23}$$

Then

$$\bar{r}' = x'\hat{x} + y'\hat{y} + z'\hat{z} = x'\hat{x} + y'\hat{y} + \left[p_{3n}x' + q_{3n}y' + f_{12}(x', y')\right]\hat{z} \tag{24}$$

The term $p_{3n}x' + q_{3n}y'$ accounts for the slope of the planar patch while $f_{12}(x', y')$ accounts for the stochastic roughness/topography. The electric field of the incidence plane wave on the patch is:

$$\overline{E}_i\left(\bar{r}'\right) = \hat{e}_{in}E_0 \exp\left(ikR_{nt}\right)\exp\left(i\bar{k}_{in} \cdot \bar{r}'\right) \tag{25}$$

in which the term $\exp(ikR_{nt})$ accounts for the phase at the center of the patch. The plane wave phase term $\exp(i\bar{k}_{in} \cdot \bar{r}')$ accounts for the phase at a point $\bar{r}'$ on the rough surface relative to the patch center. The amplitude E_0 is

$$E_0 = \frac{1}{R_{nt}}\sqrt{\frac{\eta P_t G_t}{2\pi}} \tag{26}$$

where η is the wave impedance of 377 Ohms, and P_t and G_t are the power and gain of the transmitter, respectively. The scattered wave to the receiver has the wave vector:

$$\begin{aligned}
\hat{k}_{sn} &= k_{snx}\hat{x} + k_{sny}\hat{y} + k_{snz}\hat{z} \\
k_{snx} &= \frac{k(x_r - x_n)}{R_{nr}} \\
k_{sny} &= -\frac{ky_n}{R_{nr}} \\
k_{snz} &= \frac{k(h_r - z_n)}{R_{nr}}
\end{aligned} \tag{27}$$

The polarizations of the scattered waves are $\hat{h}_{sn}$ and $\hat{v}_{sn}$, where

$$\begin{aligned}
\hat{h}_{sn} &= \frac{\hat{z} \times \hat{k}_{sn}}{\left|\hat{z} \times \hat{k}_{sn}\right|} = \frac{-k_{sny}\hat{x} + k_{sny}\hat{y}}{\sqrt{k_{sny}^2 + k_{sny}^2}} \\
\hat{v}_{sn} &= \hat{h}_{sn} \times \hat{k}_{sn}
\end{aligned} \tag{28}$$

The electric field of the scattered wave is:

$$\bar{E}_{sn} = \frac{ik \exp\left(ik\left(R_{nt} + R_{nr}\right)\right)}{4\pi R_{nt}R_{nr}}\sqrt{\frac{\eta P_t G_t}{2\pi}}\left(\hat{v}_{sn}\hat{v}_{sn} + \hat{h}_{sn}\hat{h}_{sn}\right) \cdot \int\limits_{\text{patch}} dx'dy' \exp\left(i\bar{k}_{dn} \cdot \bar{r}'\right)\overline{F}\left(\alpha, \beta\right) \tag{29}$$

where

$$\bar{k}_{dn} = \bar{k}_{in} - \bar{k}_{sn} = k_{dxn}\hat{x} + k_{dyn}\hat{y} + k_{dzn}\hat{z} \tag{30}$$

The phase term in the integrand is then

$$\exp\left(i\bar{k}_{dn} \cdot \bar{r}\right) = \exp\left\{i\left[(k_{dxn} + k_{dnz}p_{3n})x' + (k_{dyn} + k_{dnz}q_{3n})y' + k_{dnz}f_{12}\left(x', y'\right)\right]\right\} \tag{31}$$

In the above equation,

$$\begin{aligned}
\overline{F}\left(\alpha, \beta\right) = \sqrt{1 + \alpha^2 + \beta^2}&\left\{R_{hn}\left(\hat{e}_{in} \cdot \hat{q}_{in}\right)\left(\hat{n}_n \cdot \hat{k}_{in}\right)\hat{q}_{in} + R_{vn}\left(\hat{e}_{in} \cdot \hat{p}_{in}\right)\left(\hat{n}_n \times \hat{q}_{in}\right)\right. \\
&\left. + R_{hn}\left(\hat{e}_{in} \cdot \hat{q}_{in}\right)\left(\hat{k}_{sn} \times \left(\hat{n}_n \times \hat{q}_{in}\right)\right) - R_{vn}\left(\hat{e}_{in} \cdot \hat{p}_{in}\right)\left(\hat{n}_n \cdot \hat{k}_{in}\right)\left(\hat{k}_{sn} \times \hat{q}_{in}\right)\right\}
\end{aligned} \tag{32}$$

where α and β are the slopes of $f(x, y)$ in the x and y directions, respectively. The local coordinate system is expressed as:

$$\begin{aligned}
\hat{n}_n &= \frac{-\alpha\hat{x} - \beta\hat{y} + \hat{z}}{\sqrt{\alpha^2 + \beta^2 + 1}} \\
\hat{q}_{in} &= \frac{\hat{k}_{in} \times \hat{n}_n}{\left|\hat{k}_{in} \times \hat{n}_n\right|} \\
\hat{p}_{in} &= \hat{q}_{in} \times \hat{k}_{in}
\end{aligned} \tag{33}$$

The local incident angle relative to the planar patch slope is:

$$\cos \theta_{lin} = -\hat{n}_n \cdot \hat{k}_{in} \tag{34}$$

The Fresnel reflection coefficients are given by:

$$
\begin{aligned}
R_{hn} &= \frac{k \cos \theta_{lin} - \sqrt{k_1^2 - k^2 \sin^2 \theta_{lin}}}{k \cos \theta_{lin} + \sqrt{k_1^2 - k^2 \sin^2 \theta_{lin}}} \\
R_{vn} &= \frac{\varepsilon_1 k \cos \theta_{lin} - \varepsilon \sqrt{k_1^2 - k^2 \sin^2 \theta_{lin}}}{\varepsilon_1 k \cos \theta_{lin} + \varepsilon \sqrt{k_1^2 - k^2 \sin^2 \theta_{lin}}}
\end{aligned}
\tag{35}
$$

where ε_1 is the soil permittivity, and $k_1 = \omega \sqrt{\mu \varepsilon_1}$ is the wavenumber in the soil. We note that in the Kirchhoff integral, the phase factor $\exp(i\bar{k}_{dn} \cdot \bar{r}')$ is based on single scattering approximation assuming that the phase of the electric field and the magnetic field at $\bar{r}'$ are the same as that of the incident wave. The factor $\overline{F}(\alpha, \beta)$ is a result of the tangent plane approximation so that the directions and magnitudes of the tangential electric field and the tangential magnetic field are that existing on the tangent plane. Since analytical Kirchhoff approach means to get an analytical solution, we need to make an approximation to the factor $\overline{F}(\alpha, \beta)$. We make a small slope approximation so that

$$\overline{F}(\alpha, \beta) \simeq \overline{F}(p_{3n}, q_{3n}) \tag{36}$$

Then we have:

$$\bar{E}_{sn} = \sqrt{A} \frac{i \exp\left(ik\left(R_{nt} + R_{nr}\right)\right)}{4\pi R_{nt} R_{nr}} \sqrt{\frac{\eta P_t G_t}{2\pi}} \left[\hat{v}_{sn} \left(\hat{v}_{sn} \cdot \overline{F}(p_{3n}, q_{3n})\right) + \hat{h}_{sn} \left(\hat{h}_{sn} \cdot \overline{F}(p_{3n}, q_{3n})\right) \right] I_n^{(N)} \tag{37}$$

where the normalized dimensionless integral $I_n^{(N)}$ is:

$$I_n^{(N)} = \frac{k}{\sqrt{A}} \int\limits_{\text{patch}} dx' dy' \exp\left\{ i\left[(k_{dxn} + k_{dnz} p_{3n}) x' + (k_{dyn} + k_{dnz} q_{3n}) y' + k_{dnz} f_{12}\left(x', y'\right) \right] \right\} \tag{38}$$

In the above equation, $A = L^2$ is the area of the patch. We use a slightly different definition from page 80 of Reference [12] as we make $I_n^{(N)}$ dimensionless. In Reference [12] we used an unnormalized integral I, which is without the $k/\sqrt{A}$ factor.

3.1. Coherent Field and Incoherent Intensity

The coherent field and incoherent intensity correspond to the average and the variance of the integral $I_n^{(N)}$. They are evaluted using methods described in page 80 of [12]. The average of $I_n^{(N)}$, denoted by $\left\langle I_n^{(N)} \right\rangle$, is expressed as:

$$\left\langle I_n^{(N)} \right\rangle = kL \exp\left(-\frac{k_{dzn}^2 h^2}{2}\right) \text{sinc}\left[\left(\frac{k_{dxn}}{k_{dzn}} + p_{3n}\right) \frac{k_{dzn} L}{2} \right] \text{sinc}\left[\left(\frac{k_{dyn}}{k_{dzn}} + q_{3n}\right) \frac{k_{dzn} L}{2} \right] \tag{39}$$

where $L = 30\,\text{m}$ is the planar patch size of DEM $f_3(x, y)$. The variance of $I_n^{(N)}$ is, assuming isotropic roughness and isotropic fine scale topography of f_{12}:

$$
\begin{aligned}
D_{I_n}^{(N)} &= \left\langle \left| I_n^{(N)} \right|^2 \right\rangle - \left| \left\langle I_n^{(N)} \right\rangle \right|^2 \\
&= 2\pi k^2 \int_0^\infty d\rho \rho J_0\left(\rho \sqrt{(k_{dxn} + k_{dzn} p_{3n})^2 + (k_{dyn} + k_{dzn} q_{3n})^2} \right) \\
&\quad \cdot \left\{ \exp\left[-k_{dzn}^2 h^2 \left(1 - C(\rho)\right) \right] - \exp\left(-k_{dzn}^2 h^2\right) \right\}
\end{aligned}
\tag{40}
$$

Note that Eq. (40) is well behaved even if $k_{dzn}^2 h^2$ is large, since $1 - C(\rho)$ can be small. From Eqs. (37) and (38), the coherent field is:

$$
\langle \overline{E}_{sn} \rangle = \sqrt{A} \frac{i \exp\left(ik\left(R_{nt} + R_{nr}\right)\right)}{4\pi R_{nt} R_{nr}} \sqrt{\frac{\eta P_t G_t}{2\pi}}
$$
$$
\cdot \left[\hat{v}_{sn} \left(\hat{v}_{sn} \cdot \overline{F}(p_{3n}, q_{3n}) \right) + \hat{h}_{sn} \left(\hat{h}_{sn} \cdot \overline{F}(p_{3n}, q_{3n}) \right) \right] \langle I_n^{(N)} \rangle \tag{41}
$$

Then we can obtain the coherent intensity:

$$
\left| \langle \overline{E}_{sn} \rangle \right|^2 = \frac{\eta A P_t G_t}{32\pi^3 R_{nt}^2 R_{nr}^2} \left[\left| \hat{v}_{sn} \cdot \overline{F}(p_{3n}, q_{3n}) \right|^2 + \left| \hat{h}_{sn} \cdot \overline{F}(p_{3n}, q_{3n}) \right|^2 \right] \left| \langle I_n^{(N)} \rangle \right|^2 \tag{42}
$$

From Eqs. (37) and (40), we can also obtain the incoherent intensity:

$$
\left| \varepsilon_{sn} \right|^2 = \frac{\eta A P_t G_t}{32\pi^3 R_{nt}^2 R_{nr}^2} \left[\left| \hat{v}_{sn} \cdot \overline{F}(p_{3n}, q_{3n}) \right|^2 + \left| \hat{h}_{sn} \cdot \overline{F}(p_{3n}, q_{3n}) \right|^2 \right] D_{I_n}^{(N)} \tag{43}
$$

In this paper, we numerically illustrate the bistatic scattering coefficients γ defined by:

$$
\gamma = \frac{(4\pi)^2 R_t^2 R_r^2}{2\eta P_t G_t A \cos\theta_i} |E_s|^2 \tag{44}
$$

which is normalized by the single patch area $A = L^2$. Then

$$
\gamma_{n,\,\mathrm{coh}} = \frac{1}{4\pi \cos\theta_i} \left[\left| \hat{v}_{sn} \cdot \overline{F}(p_{3n}, q_{3n}) \right|^2 + \left| \hat{h}_{sn} \cdot \overline{F}(p_{3n}, q_{3n}) \right|^2 \right] \left| \langle I_n^{(N)} \rangle \right|^2
$$
$$
\gamma_{n,\,\mathrm{incoh}} = \frac{1}{4\pi \cos\theta_i} \left[\left| \hat{v}_{sn} \cdot \overline{F}(p_{3n}, q_{3n}) \right|^2 + \left| \hat{h}_{sn} \cdot \overline{F}(p_{3n}, q_{3n}) \right|^2 \right] D_{I_n}^{(N)}
\tag{45}
$$

3.2. Simplifications Based on Small Slopes

It should be noted that in GNSS-R the scattering is close to the specular direction. Furthermore, major contributions of scattered power arise from areas of small slopes. Thus, the Fresnel reflection coefficients are the values close to incident direction θ_{in} as the corrections to local incident angle are small. Using the small slope approximation and assuming incident right hand circular polarized waves (RHCP), we have:

$$
\hat{v}_{sn} \left(\hat{v}_{sn} \cdot \overline{F}(p_{3n}, q_{3n}) \right) + \hat{h}_{sn} \left(\hat{h}_{sn} \cdot \overline{F}(p_{3n}, q_{3n}) \right) = (-2\cos\theta_i) \frac{\hat{v}_{sn} R_v(\theta_{in}) + i\hat{h}_{sn} R_h(\theta_{in})}{\sqrt{2}} \tag{46}
$$

Thus, Eq. (45) can be simplified as:

$$
\gamma_{n,\,\mathrm{coh}} = \frac{\cos\theta_i}{\pi} \left[\frac{|R_v(\theta_{in})|^2 + |R_h(\theta_{in})|^2}{2} \right] \left| \langle I_n^{(N)} \rangle \right|^2
$$
$$
\gamma_{n,\,\mathrm{incoh}} = \frac{\cos\theta_i}{\pi} \left[\frac{|R_v(\theta_{in})|^2 + |R_h(\theta_{in})|^2}{2} \right] D_{I_n}^{(N)}
\tag{47}
$$

4. MULTIPLE DEM 30-METER PLANAR PATCHES

For the land surface which is divided into multiple DEM patches with size of L (e.g., $L = 30$ meters), the coherent fields are obtained by field summation from each patch. The incoherent intensity is obtained by incoherent summation from each patch. Let there be N patches.

4.1. Coherent

The total coherent field is expressed as:

$$\left\langle \overline{E}_s \right\rangle = \sum_{n=1}^{N} \frac{iL \exp\left[ik\left(R_{nt} + R_{nr}\right)\right]}{4\pi R_{nt} R_{nr}} \sqrt{\frac{\eta P_t G_t}{2\pi}} \left(\hat{v}_{sn}\hat{v}_{sn} + \hat{h}_{sn}\hat{h}_{sn}\right) \cdot \overline{F}(p_{3n}, q_{3n}) \left\langle I_n^{(N)} \right\rangle \tag{48}$$

in which

$$R_{nt} + R_{nr} = \sqrt{(x_n - x_t)^2 + y_n^2 + (z_n - h_t)^2} + \sqrt{(x_n - x_r)^2 + y_n^2 + (z_n - h_r)^2} \tag{49}$$

The phase term of $\exp[ik(R_{nt} + R_{nr})]$ depends on $(R_{nt} + R_{nr})$, which is the total distance from the transmitter to the center of 30 m patch (x_n, y_n, z_n), and from patch center to the receiver. Since the 30 m $f_3(x, y)$ is a deterministic quantity, the patch center (x_n, y_n, z_n) is also deterministic. The average is required for the term $\exp[ik(R_{nt} + R_{nr})]$.

From Eq. (48), the coherent intensity is, summing the complex field first before absolute value square

$$\left| \left\langle \overline{E}_s \right\rangle \right|^2 = L^2 \frac{\eta P_t G_t}{2\pi} \left| \sum_{n=1}^{N} \frac{\exp\left[ik\left(R_{nt} + R_{nr}\right)\right]}{4\pi R_{nt} R_{nr}} \left(\hat{v}_{sn}\hat{v}_{sn} + \hat{h}_{sn}\hat{h}_{sn}\right) \cdot \overline{F}(p_{3n}, q_{3n}) \left\langle I_n^{(N)} \right\rangle \right|^2 \tag{50}$$

The bistatic scattering coefficients are normalized by the area $A = NL^2$. For the coherent γ, we have:

$$\gamma_{\text{coh}} = \frac{R_t^2 R_r^2}{4N\pi \cos\theta_i} \left| \sum_{n=1}^{N} \frac{\exp\left[ik\left(R_{nt} + R_{nr}\right)\right]}{R_{nt} R_{nr}} \left(\hat{v}_{sn}\hat{v}_{sn} + \hat{h}_{sn}\hat{h}_{sn}\right) \cdot \overline{F}(p_{3n}, q_{3n}) \left\langle I_n^{(N)} \right\rangle \right|^2 \tag{51}$$

In the above equation, the key term of the coherent effect is $\exp[ik(R_{nt} + R_{nr})] \left\langle I_n^{(N)} \right\rangle$, as the elevation differences of the patch will create last fluctuations in the complex value of $\exp[ik(R_{nt} + R_{nr})] \left\langle I_n^{(N)} \right\rangle$. The rest of the terms, $\frac{1}{R_{nt} R_{nr}}(\hat{v}_{sn}\hat{v}_{sn} + \hat{h}_{sn}\hat{h}_{sn}) \cdot \overline{F}(p_{3n}, q_{3n})$, only have small variations from patch to patch. Using small slope approximations as in Eq. (46), Eq. (51) can be simplified as:

$$\gamma_{\text{coh}} = \frac{R_t^2 R_r^2 \cos\theta_i}{N\pi} \left| \sum_{n=1}^{N} \frac{\exp\left[ik\left(R_{nt} + R_{nr}\right)\right]}{R_{nt} R_{nr}} \frac{\hat{v}_{sn} R_v(\theta_{in}) + i\hat{h}_{sn} R_h(\theta_{in})}{\sqrt{2}} \left\langle I_n^{(N)} \right\rangle \right|^2 \tag{52}$$

To calculate the coherent γ within a certain area, we need first to obtain the coherent field from each patch using Eq. (41). Then we obtain the total coherent field from the area by the complex summation of the coherent field over patches with Eq. (48). After that, we can calculate the coherent intensity of the area with Eq. (50) and then get the coherent γ using Eq. (51) or Eq. (52).

4.2. Incoherent

The total incoherent intensity is by incoherent intensity summation:

$$|\varepsilon_s|^2 = \sum_{n=1}^{N} \frac{\eta L^2 P_t G_t}{32\pi^3 R_{nt}^2 R_{nr}^2} \left[\left|\hat{v}_{sn} \cdot \overline{F}(p_{3n}, q_{3n})\right|^2 + \left|\hat{h}_{sn} \cdot \overline{F}(p_{3n}, q_{3n})\right|^2 \right] D_{I_n}^{(N)} \tag{53}$$

For the incoherent γ, we have:

$$\gamma_{\text{incoh}} = \frac{R_t^2 R_r^2}{4N\pi \cos\theta_i} \sum_{n=1}^{N} \frac{1}{R_{nt}^2 R_{nr}^2} \left[\left|\hat{v}_{sn} \cdot \overline{F}(p_{3n}, q_{3n})\right|^2 + \left|\hat{h}_{sn} \cdot \overline{F}(p_{3n}, q_{3n})\right|^2 \right] D_{I_n}^{(N)} \tag{54}$$

In Eq. (51) and (54), R_t and R_r are the distances from the area center to the receiver and transmitter, respectively. Similarly, using small slope approximations as in Eq. (46), Eq. (54) can be simplified as:

$$\gamma_{\text{incoh}} = \frac{R_t^2 R_r^2 \cos\theta_i}{N\pi} \sum_{n=1}^{N} \frac{1}{R_{nt}^2 R_{nr}^2} \left[\frac{|R_v(\theta_{in})|^2 + |R_h(\theta_{in})|^2}{2} \right] D_{I_n}^{(N)} \tag{55}$$

To calculate the incoherent γ within a certain area, the incoherent intensity from each patch is computed with Eq. (43). Then the total incoherent intensity is obtained by using Eq. (53). Finally, we can calculate the incoherent γ of the area with Eq. (54) or Eq. (55).

5. FORMULAS OF NUMERICAL KIRCHHOFF AND FINE SCALE PARTIAL COHERENT PATCH MODEL

We will compare the AKS results with Numerical Kirchhoff Approach (NKA) and Fine Scale Partial Coherent Patch (FPCP) model. The derivations of NKA are in Reference [19]. The derivations of FPCP are in Reference [20] followed by Reference [21].

Below we summarize the equations of NKA and FPCP models. NKA results are treated as benchmark as it gives the exact solution due to Kirchhoff approximation to the entire problem of $f(x,y) = f_{12}(x,y) + f_3(x,y)$. In the NKA, a 2 cm discretization is used for numerical integration of Kirchhoff integral. At such fine discretization, both f_1 and f_2 are treated as random processes. Monte Carlo simulations are taken over realizations of f_1 and f_2 (Table 1). The integration is over an area A. The ensemble average angular bracket is over both f_1 and f_2. Let $\bar{r}_c$ be the center of the area. The total bistatic scattering coefficient is:

$$\gamma_{\text{tot}} = \frac{k^2}{4\pi A \cos\theta_i} \left\langle \left| \iint dS' \left(\bar{\bar{I}} - \hat{k}_s \hat{k}_s \right) \cdot \overline{F}(\alpha,\beta) \exp\left[i\bar{k}_d \cdot \left(\bar{r}' - \bar{r}_c \right) \right] \right|^2 \right\rangle \tag{56}$$

The coherent bistatic scattering coefficient is:

$$\gamma_{\text{coh}} = \frac{k^2}{4\pi A \cos\theta_i} \left| \left\langle \iint dS' \left(\bar{\bar{I}} - \hat{k}_s \hat{k}_s \right) \cdot \overline{F}(\alpha,\beta) \exp\left[i\bar{k}_d \cdot \left(\bar{r}' - \bar{r}_c \right) \right] \right\rangle \right|^2 \tag{57}$$

Since the area A can be large, $\hat{k}_s$, α, β, and $\bar{k}_d$ in the above equations are treated as variables and dependent on $\bar{r}'$. The incoherent bistatic scattering coefficient is the difference between the total and the coherence:

$$\gamma_{\text{incoh}} = \gamma_{\text{tot}} - \gamma_{\text{coh}} \tag{58}$$

For the fine scale partial coherent patch model, we use fine scale patch size of

$$L_m = 1\,\text{m or } 2\,\text{m} \tag{59}$$

We use combined $f_{23}(x,y) = f_2(x,y) + f_3(x,y)$. We assume that the correlation length of f_2 is much larger than $L_m = 1\,\text{m}$. If that is not true, we reduce the size of L_m to 0.5 m, etc. Then for the patch size of $L_m = 1\,\text{m}$, the combined $f_{23}(x,y)$ is treated as planar. The slopes p_m and q_m are the slopes $f_2 + f_3$ so that $p_m = p_{2m} + p_{3m}$ and $q_m = q_{2m} + q_{3m}$.

The L_m patch has the microwave roughness $f_1(x,y)$ superimposed on it. Analytical averages of rough surface scattering theory are taken over $f_1(x,y)$. Monte Carlo simulations are taken over the random process $f_2(x,y)$ (Table 1). The angular bracket represents ensemble averaging over realizations of f_2:

$$\langle I_m \rangle = A_m \exp\left(-2k^2 h_1^2 \cos\theta_{im} \right) \text{sinc}\left[\left(\frac{k_{dmx}}{k_{dmz}} + p_m \right) \frac{L_m k_{dmz}}{2} \right] \text{sinc}\left[\left(\frac{k_{dmy}}{k_{dmz}} + q_m \right) \frac{L_m k_{dmz}}{2} \right]$$

$$D_{I_m} = 2\pi A_m \exp\left(-4k^2 h_1^2 \cos^2\theta_{im} \right) \int_0^\infty d\rho\rho \left\{ \exp\left[4k^2 h_1^2 \cos^2\theta_{im} C_1(\rho) \right] - 1 \right\} \tag{60}$$

$$\cdot J_0 \left(\rho k_{dmz} \sqrt{ \left(\frac{k_{dmx}}{k_{dmz}} + p_m \right)^2 + \left(\frac{k_{dmy}}{k_{dmz}} + q_m \right)^2 } \right)$$

The coherent summation over M patches is given by:

$$\gamma_{\text{coh}} = \frac{k^2}{4\pi A \cos\theta_i} \left| \left\langle \sum_{m=1}^{M} \exp\left[ik \left(R_{mt} + R_{mr} \right) \right] \left[\left(-2\cos\theta_{im} \right) \frac{\hat{v}_{sm} R_{vm} + i\hat{h}_{sm} R_{hm}}{\sqrt{2}} \right] \langle I_m \rangle \right\rangle \right|^2 \tag{61}$$

M is the total number of the fine scale patches of f_2. The subscript m denotes the parameters corresponding to each f_2 patch. The slopes p_m and q_m are the total slopes of $f_2 + f_3$. The ensemble average is over f_2.

The total field γ_{tot} includes the diffuse scattering due to f_1 as given by D_{I_m}:

$$
\gamma_{\text{tot}} = \frac{k^2}{4\pi A \cos\theta_i} \left\langle \left| \sum_{m=1}^{M} \exp\left[ik\left(R_{mt} + R_{mr}\right)\right] \left[(-2\cos\theta_{im}) \frac{\hat{v}_{sm} R_{vm} + i\hat{h}_{sm} R_{hm}}{\sqrt{2}} \right] \langle I_m \rangle \right|^2 \right\rangle
$$

$$
+ \frac{k^2}{4\pi A \cos\theta_i} \left\langle \sum_{m=1}^{M} \left[(4\cos^2\theta_{im}) \frac{|R_{vm}|^2 + |R_{hm}|^2}{2} \right] D_{I_m} \right\rangle
$$

(62)

Similarly, we can obtain the incoherence from Eq. (58).

6. GEOMETRIC OPTICS APPROACH

The geometric optics consists of making the high frequency approximation of $k \to \infty$. Since microwave roughness does not fall in that category, f_1 is first ignored. The stationary phase approximation is then applied to the Kirchhoff integral to the phase term with $f_{23}(x, y) = f_2(x, y) + f_3(x, y)$. The results are independent of frequency. In the GO-Att, an attenuation term $\exp(-4k^2 h_1^2 \cos^2\theta_i)$ is added. The approach requires the decomposition of f_{12} separately into $f_1 + f_2$. The GO was applied to GNSS-R for ocean [13]. The GO-Att was applied in reference and is also labelled as the "improved geometric optics model" [14]. In test books, GO means GO without attenuation.

6.1. Single DEM Patch

In the geometric optics approach, we start from Eq. (29). Geometric optics means that rms height of random roughness/topography is comparable or larger than the wavelength. Since $f_1(x, y)$ is microwave roughness which is much smaller than the wavelength, it will be ignored. Thus, only fine scale topography f_2 is included in GO. Thus, the application of GO requires the decomposition into f_1 and f_2.

Then the phase term is:

$$
\exp(i\bar{k}_{dn} \cdot \bar{r}') = \exp\left\{ i \left[(k_{dxn} + k_{dzn} p_{3n}) \, x' + (k_{dyn} + k_{dzn} q_{3n}) \, y' + k_{dzn} f_2(x', y') \right] \right\}
$$

$$
= \exp\left\{ i \left[\left(k_{dxn} + k_{dzn} \frac{\partial f_3}{\partial x'} \right) x' + \left(k_{dyn} + k_{dzn} \frac{\partial f_3}{\partial y'} \right) y' + k_{dzn} f_2(x', y') \right] \right\} \quad (63)
$$

Let $\frac{\partial f_2}{\partial x'} = p_2$, $\frac{\partial f_2}{\partial y'} = q_2$. Using method of stationary phase, the stationary phase point is calculated by:

$$
(k_{dxn} + k_{dzn} p_{3n}) + k_{dzn} \frac{\partial f_2}{\partial x'} = 0
$$

$$
(k_{dyn} + k_{dzn} q_{3n}) + k_{dzn} \frac{\partial f_2}{\partial y'} = 0
$$

(64)

from which we can obtain the stationary phase point:

$$
p_2 = -\left(\frac{k_{dxn}}{k_{dzn}} + p_{3n} \right)
$$

$$
q_2 = -\left(\frac{k_{dyn}}{k_{dzn}} + q_{3n} \right)
$$

(65)

For the $\overline{F}(\alpha, \beta)$ factor, we have:

$$
\alpha = \frac{\partial}{\partial x'} \left[f_2(x', y') + f_3(x', y') \right] = p_2 + p_{3n}
$$

$$
\beta = \frac{\partial}{\partial y'} \left[f_2(x', y') + f_3(x', y') \right] = q_2 + q_{3n}
$$

(66)

At the stationary phase point:

$$\alpha = \alpha_{0n} = -\frac{k_{dxn}}{k_{dzn}}$$
$$\beta = \beta_{0n} = -\frac{k_{dyn}}{k_{dzn}}$$

(67)

Then we can carry out the integration in Eq. (29) as shown below:

$$\overline{E}_{sn} = \sqrt{A}\,\frac{i\exp\left[ik(R_{nr}+R_{nt})\right]}{4\pi R_{nr}R_{nt}}\sqrt{\frac{\eta P_t G_t}{2\pi}}\left[\hat{v}_{sn}\left(\hat{v}_{sn}\cdot\overline{F}(\alpha_{0n},\beta_{0n})\right)+\hat{h}_{sn}\left(\hat{h}_{sn}\cdot\overline{F}(\alpha_{0n},\beta_{0n})\right)\right]I_n^{(N)}$$

(68)

where the normalized dimensionless integral $I_n^{(N)}$ is:

$$I_n^{(N)} = \frac{k}{\sqrt{A}}\int\limits_{\text{patch}} dx'dy'\exp\left\{i\left[(k_{dxn}+k_{dzn}p_{3n})\,x'+(k_{dyn}+k_{dzn}q_{3n})\,y'+k_{dzn}f_2(x',y')\right]\right\}$$

(69)

Taking the squared absolute value, we can obtain:

$$\left|I_n^{(N)}\right|^2 = \frac{k^2}{A}\iint dx'dy'\iint dx''dy''\exp\left\{i\left[(k_{dxn}+k_{dzn}p_{3n})\,(x'-x'')\right.\right.$$
$$\left.\left.+(k_{dyn}+k_{dzn}q_{3n})\,(y'-y'')+k_{dzn}\left(f_2(x',y')-f_2(x'',y'')\right)\right]\right\}$$

(70)

By assuming $k\to\infty$, we make Taylor expansion of f_2 so that

$$f_2(x',y')-f_2(x'',y'') = p_2(x'-x'')+q_2(y'-y'')$$

(71)

Then Eq. (70) can be written as:

$$\left|I_n^{(N)}\right|^2 = \frac{k^2}{A}\iint dx'dy'\iint dx''dy''\exp\left\{i\left[(k_{dxn}+k_{dzn}(p_2+p_{3n}))\,(x'-x'')\right.\right.$$
$$\left.\left.+(k_{dyn}+k_{dzn}(q_2+q_{3n}))\,(y'-y'')\right]\right\}$$
$$= 4\pi^2k^2\delta\left[k_{dxn}+k_{dzn}(p_2+p_{3n})\right]\delta\left[k_{dyn}+k_{dzn}(q_2+q_{3n})\right]$$

(72)

In this approach, f_3 is treated as deterministic, and f_2 is treated as random process. For random f_2, let $p_{2s}(p_2,q_2)$ be the probability density functions of the slopes of $f_2(x,y)$. Averaging $|I_n^{(N)}|^2$ over the slope distributions of $p_{2s}(p_2,q_2)$:

$$\left\langle\left|I_n^{(N)}\right|^2\right\rangle = \iint dp_2dq_2p_{2s}(p_2,q_2)4\pi^2k^2\delta\left[k_{dxn}+k_{dzn}(p_2+p_{3n})\right]\delta\left[k_{dyn}+k_{dzn}(q_2+q_{3n})\right]$$
$$= \frac{4\pi^2k^2}{k_{dzn}^2}p_{2s}\left(p_2 = -\frac{k_{dxn}}{k_{dzn}}-p_{3n},\,q_2 = -\frac{k_{dyn}}{k_{dzn}}-q_{3n}\right)$$

(73)

From Eqs. (68) and (72), the incoherent intensity and bistatic scattering coefficients are:

$$|\varepsilon_{sn}|^2 = \frac{A\eta P_t G_t}{8\pi R_{nt}^2 R_{nr}^2}\frac{k^2}{k_{dzn}^2}\left[\left|\hat{v}_{sn}\cdot\overline{F}(\alpha_{0n},\beta_{0n})\right|^2+\left|\hat{h}_{sn}\cdot\overline{F}(\alpha_{0n},\beta_{0n})\right|^2\right]$$
$$\cdot p_{2s}\left(p_2 = -\frac{k_{dxn}}{k_{dzn}}-p_{3n},\,q_2 = -\frac{k_{dyn}}{k_{dzn}}-q_{3n}\right)$$

$$\gamma^{GO} = \frac{\pi}{\cos\theta_i}\frac{k^2}{k_{dzn}^2}\left[\left|\hat{v}_{sn}\cdot\overline{F}(\alpha_{0n},\beta_{0n})\right|^2+\left|\hat{h}_{sn}\cdot\overline{F}(\alpha_{0n},\beta_{0n})\right|^2\right]$$
$$\cdot p_{2s}\left(p_2 = -\frac{k_{dxn}}{k_{dzn}}-p_{3n},\,q_2 = -\frac{k_{dyn}}{k_{dzn}}-q_{3n}\right)$$

(74)

Let the rms slope of f_2 be s_2, then

$$p_{2s}(p_2,q_2) = \frac{1}{2\pi s_2^2}\exp\left[-\frac{\alpha^2+\beta^2}{2s_2^2}\right]$$

(75)

Thus, Eq. (74) can be rewritten as:

$$\gamma^{GO} = \frac{\pi}{\cos\theta_i} \frac{k^2}{k_{dzn}^2} \frac{1}{2\pi s_2^2} \left[\left| \hat{v}_{sn} \cdot \overline{F}(\alpha_{0n}, \beta_{0n}) \right|^2 + \left| \hat{h}_{sn} \cdot \overline{F}(\alpha_{0n}, \beta_{0n}) \right|^2 \right]$$
$$\cdot \exp\left[-\frac{\left(\frac{k_{dxn}}{k_{dzn}} + p_{3n}\right)^2 + \left(\frac{k_{dyn}}{k_{dzn}} + q_{3n}\right)^2}{2s_2^2} \right] \tag{76}$$

Further simplifications are made as shown in page 84 of Reference [12]. The normal vector in $\overline{F}(\alpha_{0n}, \beta_{0n})$ is

$$\hat{n} = \frac{\bar{k}_{sn} - \bar{k}_{in}}{\left| \bar{k}_{dn} \right|} \tag{77}$$

from which we can obtain the local incident angle and Fresnel reflection coefficients:

$$\cos\theta_{lin} = -\hat{n} \cdot \hat{k}_{in} \tag{78}$$

$$R_{hn} = \frac{k\cos\theta_{lin} - \sqrt{k_1^2 - k^2\sin^2\theta_{lin}}}{k\cos\theta_{lin} + \sqrt{k_1^2 - k^2\sin^2\theta_{lin}}}$$

$$R_{vn} = \frac{\varepsilon_1 k\cos\theta_{lin} - \varepsilon\sqrt{k_1^2 - k^2\sin^2\theta_{lin}}}{\varepsilon_1 k\cos\theta_{lin} + \varepsilon\sqrt{k_1^2 - k^2\sin^2\theta_{lin}}} \tag{79}$$

For circular polarized waves,

$$\left| \hat{v}_{sn} \cdot \overline{F}(\alpha_{0n}, \beta_{0n}) \right|^2 + \left| \hat{h}_{sn} \cdot \overline{F}(\alpha_{0n}, \beta_{0n}) \right|^2 = \frac{|R_{vn}|^2 + |R_{hn}|^2}{2} \frac{\left| \bar{k}_{dn} \right|^4}{k^2 k_{dzn}^2} \tag{80}$$

Then Eq. (76) can be rewritten as:

$$\gamma^{GO} = \frac{1}{\cos\theta_i} \frac{|R_{vn}|^2 + |R_{hn}|^2}{2} \frac{\left| \bar{k}_{dn} \right|^4}{k_{dzn}^4} \frac{1}{2s_2^2} \exp\left[-\frac{\left(\frac{k_{dxn}}{k_{dzn}} + p_{3n}\right)^2 + \left(\frac{k_{dyn}}{k_{dzn}} + q_{3n}\right)^2}{2s_2^2} \right] \tag{81}$$

It should be noted that in GNSS-R the scattering is close to the specular direction. Furthermore, major contributions of scattered power arise from areas of small slopes. Thus, the Fresnel reflection coefficients are the values close to the incident direction θ_{in} as the corrections to local incidence angle are small.

Assuming Gaussian correlation function of f_2 with rms height h_2 and correlation length l_2, then $s_2^2 = 2(h_2/l_2)^2$. Thus, from Eq. (81), we obtain:

$$\gamma^{GO} = \frac{|R_{vn}|^2 + |R_{hn}|^2}{8(h_2/l_2)^2 \cos\theta_i} \frac{\left| \bar{k}_{dn} \right|^4}{k_{dzn}^4} \exp\left[-\frac{\left(\frac{k_{dxn}}{k_{dzn}} + p_{3n}\right)^2 + \left(\frac{k_{dyn}}{k_{dzn}} + q_{3n}\right)^2}{4(h_2/l_2)^2} \right] \tag{82}$$

In the models from Reference [14], a microwave roughness attenuation factor $\exp(-k_{dz}^2 h_1^2 \cos^2\theta_i)$ is attached. Then the improved Geometric Optics (GO-Att) model is:

$$\gamma^{GO\text{-}Att} = \exp\left(-4k^2 h_1^2 \cos^2\theta_i\right) \frac{|R_{vn}|^2 + |R_{hn}|^2}{8(h_2/l_2)^2 \cos\theta_i} \frac{\left| \bar{k}_{dn} \right|^4}{k_{dzn}^4} \exp\left[-\frac{\left(\frac{k_{dxn}}{k_{dzn}} + p_{3n}\right)^2 + \left(\frac{k_{dyn}}{k_{dzn}} + q_{3n}\right)^2}{4(h_2/l_2)^2} \right] \tag{83}$$

It is to be noted that:

(i) the factor $\exp\left(-4k^2 h_1^2 \cos^2 \theta_i\right)$ is significant, as shown in Table 3.

(ii) the improved GO model requires a dividing line between f_1 and f_2. For example, it is unclear whether $h_1 = 3\,\text{cm}$ should be treated as f_1 or f_2 at wavelength $= 19\,\text{cm}$. However, AKS and NKA do not need to divide between f_1 and f_2.

6.2. Multiple DEM Patches

Since GO gives the incoherent component of the scattered fields, summations of incoherent intensities are applied to multiple DEM patches. The roughness parameters h_{1n} and $(h_2/l_2)_n$ are corresponding to each nth patch.

$$\gamma^{GO} = \frac{R_t^2 R_r^2}{8N \cos \theta_i} \sum_{n=1}^{N} \frac{1}{R_{nt}^2 R_{nr}^2} \frac{|R_{vn}|^2 + |R_{hn}|^2}{(h_2/l_2)_n^2} \frac{|\bar{k}_{dn}|^4}{k_{dzn}^4} \exp\left[-\frac{\left(\dfrac{k_{dxn}}{k_{dzn}} + p_{3n}\right)^2 + \left(\dfrac{k_{dyn}}{k_{dzn}} + q_{3n}\right)^2}{4(h_2/l_2)_n^2}\right]$$

$$\gamma^{GO\text{-}Att} = \frac{R_t^2 R_r^2}{8N \cos \theta_i} \sum_{n=1}^{N} \frac{1}{R_{nt}^2 R_{nr}^2} \frac{|R_{vn}|^2 + |R_{hn}|^2}{(h_2/l_2)_n^2} \frac{|\bar{k}_{dn}|^4}{k_{dzn}^4} \exp\left[-\frac{\left(\dfrac{k_{dxn}}{k_{dzn}} + p_{3n}\right)^2 + \left(\dfrac{k_{dyn}}{k_{dzn}} + q_{3n}\right)^2}{4(h_2/l_2)_n^2}\right]$$

$$\cdot \exp\left(-4k^2 h_{1n}^2 \cos^2 \theta_{in}\right) \tag{84}$$

Note that both GO models are derived from the Kirchhoff integral based on stationary phase approximation. As shown in Table 3, with $h_1 = 3\,\text{cm}$, the results of GO models are different as much as 10 dB.

Table 3. Typical values of the attenuation factor $\exp(-4k^2 h_1^2 \cos^2 \theta_i)$ in GO-Att. $k = 33\,\text{m}^{-1}$, $\theta_i = 40°$.

h_1 (cm)	$-4k^2 h_1^2 \cos^2 \theta_i$	$\exp(-4k^2 h_1^2 \cos^2 \theta_i)$ (dB)
1.0	0.26	-1.11
2.0	1.02	-4.44
3.0	2.30	-10.0
6.0	6.39	-40.0

7. EQUATIONS FOR TRACK RESULTS AND DEM

In applying AKS to track results, we only use the incoherent intensity. The total area is large. $A_n = L^2$ is used with $L = 30\,\text{m}$. Each area patch has a p_{3n} and q_{3n} as described in Sections 2 and 3.

For the ith delay and jth Doppler bin, the ratio of scattered power to incident power is:

$$\left(\frac{P_r}{P_r}\right)_{ij} = \frac{G_t G_r}{64\pi^2 R_t^2 R_r^2} \sum_{n=1}^{N} A_n W_{ij}(n) \frac{4}{k^2} \cos^2 \theta_i \left|R_{cp}(\theta_i)\right|^2 D_{I_n}^{(N)} \tag{85}$$

where N is the total number of patches within the receiver antenna footprint. Each CYGNSS DDM collects the scattered signal within a circle with radius of 50 km centered at specular point corresponding to

$$N = 8 \times 10^6$$

$30\,\text{m} \times 30\,\text{m}$ patches.

$$\left|R_{cp}(\theta_i)\right|^2 = \frac{|R_{vn}|^2 + |R_{hn}|^2}{2} \tag{86}$$

$$D_{I_n}^{(N)} = 2\pi k^2 \int_0^\infty d\rho \rho J_0 \left(\rho \sqrt{(k_{dxn} + k_{dzn} p_{3n})^2 + (k_{dyn} + k_{dzn} q_{3n})^2} \right)$$
$$\cdot \left\{ \exp\left[-k_{dzn}^2 h^2 \left(1 - C(\rho) \right) \right] - \exp\left(-k_{dzn}^2 h^2 \right) \right\} \tag{87}$$

For each patch, there is an $h^2 C(\rho)$ term. For the simulation, we let f_1 be an exponential correlation function and f_2 be a Gaussian correlation function. That is:

$$h^2 C(\rho) = h_1^2 \exp\left(-\frac{|\rho|}{l_1} \right) + h_2^2 \exp\left(-\frac{\rho^2}{l_2^2} \right) \tag{88}$$

and

$$W_{ij}(n)$$

is the weighting function value on nth patch from Reference [13]. For a given patch in the observing area, the weighting function value varies according to the different delay and Doppler bin. The bistatic radar cross section (BRCS) for the ijth delay Doppler bin is obtained by radar equation:

$$\left(\frac{P_r}{P_t} \right)_{ij} = \frac{G_t}{4\pi R_t^2} \sigma_{ij}^{\mathrm{BRCS}} \frac{1}{4\pi R_r^2} \frac{\lambda^2 G_r}{4\pi}$$
$$\sigma_{ij}^{\mathrm{BRCS}} = \left(\frac{P_r}{P_t} \right)_{ij} \frac{(4\pi)^3 R_t^2 R_r^2}{\lambda^2 G_t G_r} \tag{89}$$

BRCS is defined to describe the cross-sectional area of a perfectly reflecting sphere that would produce the same strength reflection as the scattered object. The relationship between the BRCS $\sigma_{ij}^{\mathrm{BRCS}}$ and the total bistatic scattering coefficient γ is shown in Eq. (90), in which A is the total area, and θ_i the incident angle.

$$\sigma_{ij}^{\mathrm{BRCS}} = \gamma A \cos \theta_i \tag{90}$$

8. RESULTS FOR L BAND: COHERENT AND INCOHERENT WAVES

In the simulations of the L band results, we use $freq = 1.575\,\mathrm{GHz}$, $\lambda = 0.19\,\mathrm{m}$, and $k = 33\,\mathrm{m}^{-1}$. The incident angle is $\theta_i = 40°$ except stated otherwise. For GNSS-R applications, the heights of the transmitters and receivers are:

$$h_t = 20200\,\mathrm{km}$$
$$h_r = 500\,\mathrm{km}$$

From Eqs. (7) and (8), we have:

$$x_s = h_t \tan \theta_i = 16950\,\mathrm{km}$$
$$x_r = h_r \tan \theta_s = 420\,\mathrm{km}$$

in which $\theta_s = \theta_i = 40°$ since the receiver is in the specular direction. Thus, the coordinates of the transmitter and the receiver are:

$$\mathrm{Tx} = (-16950, 0, 20200)\,\mathrm{km}$$
$$\mathrm{Rx} = (+420, 0, 500)\,\mathrm{km} \tag{91}$$

Unless specified, f_{12} is separated into

$$f_{12} = f_1 + f_2 \tag{92}$$

with f_1 governed by an exponential correlation function and f_2 by a Gaussian correlation function. The dependence on roughness/topography is contained in the two analytical expressions (Eqs. (38) and (40)), which are repeated below:

$$\left\langle I_n^{(N)} \right\rangle = kL \exp\left(-\frac{k_{dzn}^2 h^2}{2} \right) \mathrm{sinc}\left[\left(\frac{k_{dxn}}{k_{dzn}} + p_{3n} \right) \frac{k_{dzn} L}{2} \right] \mathrm{sinc}\left[\left(\frac{k_{dyn}}{k_{dzn}} + q_{3n} \right) \frac{k_{dzn} L}{2} \right]$$
$$D_{I_n}^{(N)} = 2\pi k^2 \int_0^\infty d\rho \rho J_0 \left(\rho \sqrt{(k_{dxn} + k_{dzn} p_{3n})^2 + (k_{dyn} + k_{dzn} q_{3n})^2} \right)$$
$$\cdot \left\{ \exp\left[-k_{dzn}^2 h^2 \left(1 - C(\rho) \right) \right] - \exp\left(-k_{dzn}^2 h^2 \right) \right\} \tag{93}$$

For the coherent wave, there is an exponential decay term $\exp\left(-\frac{k_{dzn}^2 h^2}{2}\right)$. The coherent wave has a sharp peak due to the sinc functions with angular width controlled by $\left(\frac{k_{dxn}}{k_{dzn}} + p_{3n}\right)$ and $\left(\frac{k_{dyn}}{k_{dzn}} + q_{3n}\right)$. The coherent waves are added coherently with complex field summations with multiple patches. For the incoherent wave, there is a dependence on $\sqrt{(k_{dxn} + k_{dzn}p_{3n})^2 + (k_{dyn} + k_{dzn}q_{3n})^2}$, which contributes to the J_0 oscillatory function. $D_{I_n}^{(N)}$ depends on the factor $\exp[-k_{dzn}^2 h^2(1 - C(\rho))]$. The term $\exp(-k_{dzn}^2 h^2)$ can be neglected. The correlation function $C(\rho)$ is also related to the spectral density. At L band, the incident angle $\theta_i = 40°$, and the scattering angle is close to specular direction, $|k_{dzn}| = 2k\cos\theta_i = 50.57\,\mathrm{m}^{-1}$.

8.1. Validation of AKS for Both Coherent Wave and Incoherent Wave

We first validate the AKS results by comparing with results of NKA and FPCP models. The surface parameters are set as:

$$h_1 = 1.0\,\mathrm{cm}, \quad l_1 = 10\,\mathrm{cm}$$
$$h_2 = 4.5\,\mathrm{cm}, \quad l_2 = 3\,\mathrm{m}$$
$$h = \sqrt{h_1^2 + h_2^2} = 4.61\,\mathrm{cm}$$
$$h^2 C(\rho) = h_1^2 \exp\left(-\frac{\rho}{l_1}\right) + h_2^2 \exp\left(-\frac{\rho^2}{l_2^2}\right)$$
$$s_2 = \frac{\sqrt{2}h_2}{l_2} = 1.21°$$

For this case, $|k_{dzn}h| = 2.33$. The simulation results are shown in Figs. 3 to 5. In Figs. 3 and 4, we have the center of the DEM patch at the specular point:

$$(x_n, y_n, z_n) = (0, 0, 0) \tag{94}$$

In Fig. 3, we compare the results for a DEM patch with $L = 30\,\mathrm{m}$ that is horizontal with zero slopes $p_{3n} = q_{3n} = 0$. The results are plotted as a function of scattered angle θ_s, which means k_{dxn} and k_{dyn} vary with θ_s. As is shown, the three results are in good agreement for both coherent waves and incoherent waves, showing that the AKS and the FPCP results are valid for both coherent and
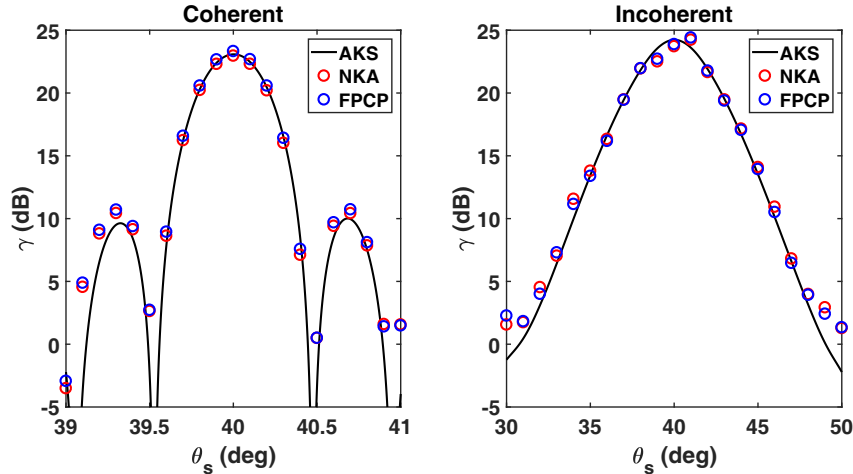

Figure 3. Bistatic scattering coefficients γ for a 30 m DEM patch with scattering angle θ_s at L band. $h_1 = 1.0\,\mathrm{cm}$, $h_2 = 4.5\,\mathrm{cm}$, $l_1 = 10\,\mathrm{cm}$, $l_2 = 3\,\mathrm{m}$.
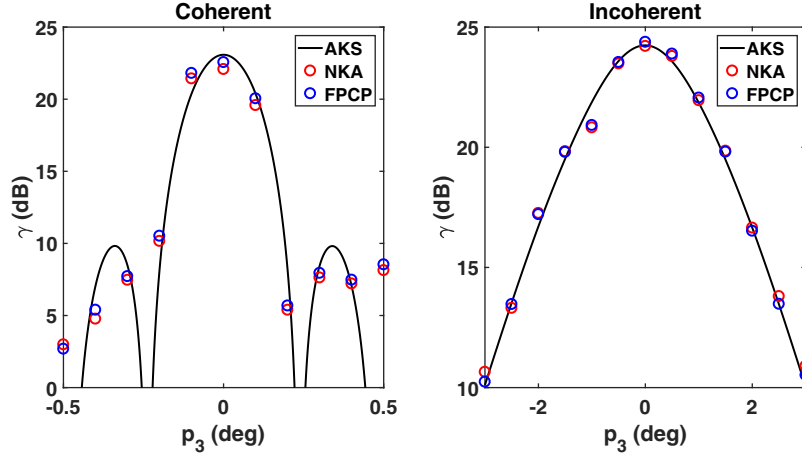
Figure 4. Bistatic scattering coefficients γ for a 30 m DEM patch with patch slope p_3 in x direction at L band. $h_1 = 1.0$ cm, $h_2 = 4.5$ cm, $l_1 = 10$ cm, $l_2 = 3$ m.
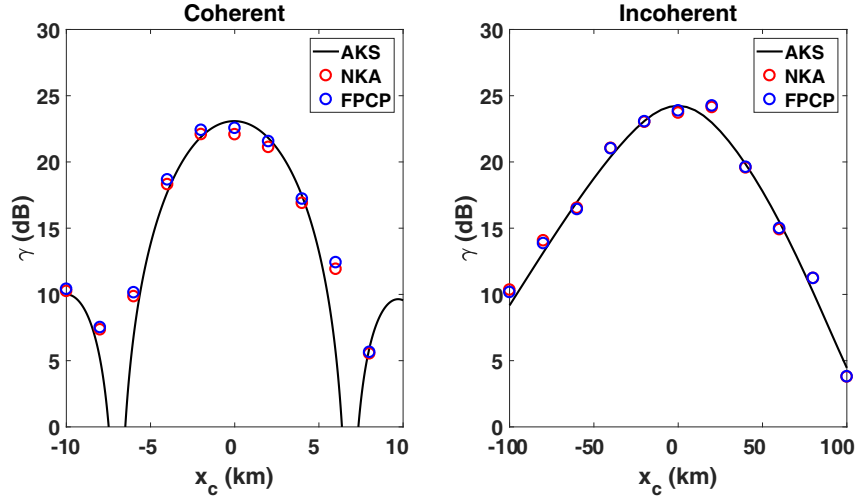

Figure 5. Bistatic scattering coefficients γ for a 30 m DEM patch with patch position x_c in x direction at L band. $h_1 = 1.0$ cm, $h_2 = 4.5$ cm, $l_1 = 10$ cm, $l_2 = 3$ m.

incoherent waves. The magnitudes of coherent and incoherent are comparable. The angular width is due to sinc $\left(\frac{k_{dxn}L}{2} \right)$. For $L = 30$ m, we have $kL/2 = 495$. We roughly approximate sinc $\left(\frac{k_{dxn}L}{2} \right)$ as:

$$\mathrm{sinc}\left(\frac{k_{dxn}L}{2} \right) = \mathrm{sinc}\left[495 \left(\sin\theta_i - \sin\theta_s \right) \right] = \mathrm{sinc}\left[379 \left(\theta_i - \theta_s \right) \right]$$

from which we notice that the angular width is approximately $1/379 = 0.15°$. For the incoherent waves, since $\sqrt{(k_{dxn} + k_{dzn}p_{3n})^2 + (k_{dyn} + k_{dzn}q_{3n})^2} = 0$ for this case, the angular width is due to the slope s_2 of the fine scale topography f_2.

In Fig. 4, we keep $\theta_s = 40°$, and plot γ as a function of p_{3n} with $q_{3n} = 0$. The three results are in good agreement, showing that the AKS and the FPCP results are valid. The magnitudes of coherent and incoherent are comparable. Since $\left(\frac{k_{dxn}}{k_{dzn}} + p_{3n} \right) \frac{k_{dzn}L}{2} = 758 p_{3n}$ the angular width of the coherent wave is $p_3 = 1/758 = 0.076°$. For the incoherent waves, since $k_{dzn}p_{3n} = 50.57 p_{3n}$ is still small, the angular width due to slope s_2 and the angular width is similar to Fig. 3.

In Fig. 5, we keep $p_{3n} = q_{3n} = 0$. γ is plotted as a function of x_c, with patch center at $(x_c, 0, 0)$.

The expression of the incidence angle and scattering angle:

$$\tan\theta_i = \frac{k_{inx}}{k_{inz}} = \frac{x_c - x_t}{h_t}$$
$$\tan\theta_s = \frac{k_{snx}}{k_{snz}} = \frac{x_r - x_c}{h_r}$$

(95)

By changing the position of the area, the incidence and scattering angle would vary correspondingly. As we move the area from $x_c = -50\,\mathrm{km}$ to $+50\,\mathrm{km}$, based on Eq. (91) and Eq. (95), the ranges of the angles are:

$$\theta_i : \ 39.92° \text{ to } 40.08°$$
$$\theta_s : \ 43.23° \text{ to } 36.50°$$

Since the transmitter height is large, the incidence angle θ_i does not change. However, the scattering angle θ_s is changing in a wider range, which is due to the relatively low height of the receiver. Thus, this case can be roughly regarded as keeping the incident angle and varying the scattering angle, which is similar to Fig. 3. Since θ_s departs from $\theta_i = 40°$ when moving away from the origin $(0, 0, 0)$, there is a peak at the position $x_c = 0\,\mathrm{km}$. According to the analysis of Fig. 3, we know that the width of x_c for coherent waves should be correlated to the angular width $\theta_s = 0.15°$. That is:

$$x_c^- = 420 - 500\tan(40° + 0.15°) = -1.8\,\mathrm{km}$$
$$x_c^+ = 420 - 500\tan(40° - 0.15°) = +2.7\,\mathrm{km}$$

(96)

which means that the width in x_c for coherent waves is from $x_c = -1.8\,\mathrm{km}$ to $+2.7\,\mathrm{km}$. The results for incoherent waves are also similar to that of Fig. 3.

As a conclusion of all the three cases above, we can find that the peak would appear when the area is horizontal and located at the specular point $(0, 0, 0)$, and when we are receiving the scattered waves at the specular direction with respect to the specular point. Moving away from this condition, the bistatic scattering coefficients would decrease for both coherence and incoherence. With the surface parameters applied above, the peak value is approximately $\gamma_{\mathrm{coh}} = 23\,\mathrm{dB}$, and $\gamma_{\mathrm{incoh}} = 24\,\mathrm{dB}$.

8.2. Coherent Waves and Incoherent Waves at L Band

In this subsection, we examine the effects of the area size to the bistatic scattering coefficients γ. For this case, we keep the observing direction in the specular direction with respect to the global specular point $(0, 0, 0)$. The land is divided into 30-meter patches since the resolution of the DEM is 30 m, even if the land is totally flat. Since the AKS formula for multiple DEM patches are derived in Section 4, we can obtain the γ for multiple DEM patches with AKS. For each 30-meter patch, we can derive the coherent field and incoherent intensity using Eqs. (41) and (43). To obtain the total coherence and incoherence from multiple DEM patches, we implement field and intensity summation to obtain the total coherent field and total incoherent intensity using Eqs. (48) and (53), respectively. Finally, γ_{coh} and γ_{incoh} can be obtained with Eqs. (51) and (54). In this paper, three different sizes of the area are considered: $\sqrt{A} = 30\,\mathrm{m}$, $60\,\mathrm{m}$, and $90\,\mathrm{m}$. For $\sqrt{A} = 30\,\mathrm{m}$, there is 1 DEM patch of 30 m, and the horizontal coordinates of the patch center is $(-30\,\mathrm{m}, -30\,\mathrm{m})$. For $\sqrt{A} = 90\,\mathrm{m}$, there are 9 DEM patches of 30 m, and the horizontal coordinates of the total area center is $(0, 0)$. For the 9 patches of the three cases, the slopes p_{3n} and q_{3n} (in degree) and the DEM heights z_n (in cm) are shown in Fig. 6. In addition, the area inclusion relations of the three cases is shown as well. The figure is only for illustration. In the simulation, we are using square area with size of $\sqrt{A} = 30\,\mathrm{m}$ for each DEM patch, instead of general rectangle as illustrated. In Fig. 7, we plot the coherent and incoherent γ as a function of area size from $\sqrt{A} = 30\,\mathrm{m}$ to $90\,\mathrm{m}$. The three results of AKS, FPCP, and NKA are in good agreement, validating the accuracies of AKS and FPCP.

From Fig. 7, we notice that γ_{incoh} stays constant around $24\,\mathrm{dB}$, while γ_{coh} decreases from $18\,\mathrm{dB}$ at $\sqrt{A} = 30\,\mathrm{m}$ to $10\,\mathrm{dB}$ at $\sqrt{A} = 90\,\mathrm{m}$. According to the position geometry of the nine patches, the center of the farthest patch is $30\sqrt{2} = 42.4\,\mathrm{m}$ away from the specular point $(0, 0, 0)$, which is a small distance. According to Fig. 5, this distance would not cause a large decrease from the peak value for

z_n = 22.22 cm p_{3n} = -0.10° q_{3n} = -0.09°	z_n = 12.22 cm p_{3n} = -0.14° q_{3n} = -0.08°	z_n = 2.22 cm p_{3n} = -0.22° q_{3n} = +0.03°
z_n = 2.22 cm p_{3n} = -0.16° q_{3n} = -0.13°	z_n = 2.22 cm p_{3n} = -0.17° q_{3n} = -0.20°	z_n = -7.78 cm p_{3n} = -0.15° q_{3n} = -0.30°
z_n = -7.78 cm p_{3n} = -0.17° q_{3n} = -0.23°	z_n = -7.78 cm p_{3n} = -0.12° q_{3n} = -0.22°	z_n = -17.78 cm p_{3n} = -0.18° q_{3n} = -0.08°

Figure 6. Patch slopes p_{3n} and q_{3n} (in degree) and the DEM heights z_n (in cm) of the 9 DEM patch. γ_{coh} decreases with area. The shape of each DEM patch is square with size $\sqrt{A} = 30\,\mathrm{m}$ in simulation.
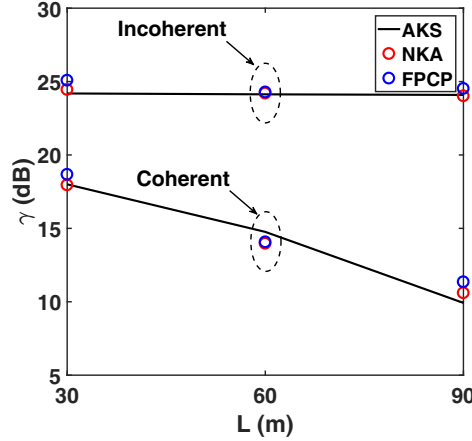
Figure 7. Bistatic scattering coefficients γ for a 30 m DEM patch with increasing area size at L band. $h_1 = 1.0\,\mathrm{cm}$, $h_2 = 4.5\,\mathrm{cm}$, $l_1 = 10\,\mathrm{cm}$, $l_2 = 3\,\mathrm{m}$.

both coherence and incoherence. All of the 9 patches can be regarded as close to the specular point. Thus, we can roughly assume that for all of the nine patches, $k_{dxn} = d_{dyn} = 0$, and $|k_{dzn}| = 50.57\,\mathrm{m}^{-1}$ as calculated previously.

For the case of $\sqrt{A} = 30\,\mathrm{m}$, γ_{coh} is 5 dB lower than the peak value 23 dB as discussed in Section 8.1. This is due to the slopes of this single patch. According to Fig. 6, this single DEM patch is tilted. The slopes are $p_{3n} = -0.10°$ and $q_{3n} = -0.09°$, which means the patch is tilted not only in x direction, but also in y direction. As is shown in Fig. 4, the coherence is sensitive to p_{3n}. Merely $p_{3n} = -0.10°$ can decrease γ_{coh} by 3 dB from the peak value. In addition, the nonzero slope q_{3n} in y direction can further decrease γ_{coh}. As a result, for the case of single DEM patch, although the patch is slightly tilted, γ_{coh} is only 18 dB, which is 5 dB lower than the peak value. As shown in Fig. 6, other patches are tilted in different directions. The slope of certain patch is as large as $|p_{3n}| = 0.30°$. The slopes of these patches contribute to the decrease of γ_{coh}. Another key factor is the phase term $\exp[ik(R_{nt} + R_{nr})]$ as shown in Eqs. (52) and (55). We rewrite the two equations as following:

$$\gamma_{\mathrm{coh}} = \frac{R_t^2 R_r^2 \cos\theta_i}{N\pi} \left| \sum_{n=1}^{N} \frac{\exp\left[ik\left(R_{nt} + R_{nr}\right)\right]}{R_{nt} R_{nr}} \frac{\hat{v}_{sn} R_v(\theta_{in}) + i\hat{h}_{sn} R_h(\theta_{in})}{\sqrt{2}} \left\langle I_n^{(N)} \right\rangle \right|^2$$

$$\gamma_{\text{incoh}} = \frac{R_t^2 R_r^2 \cos\theta_i}{N\pi} \sum_{n=1}^{N} \frac{1}{R_{nt}^2 R_{nr}^2} \left[\frac{|R_v(\theta_{in})|^2 + |R_h(\theta_{in})|^2}{2} \right] D_{I_n}^{(N)}$$

The phase term changes significantly when the position is changed, since the total distance $R_{nt}+R_{nr}$ varies from patch to patch. The variations in the phase term would cause that the scattered fields from different patch are actually not in phase. As a result, the total coherent fields and γ_{coh} decrease by increasing the area.

For the incoherence, however, the total scattered fields are calculated by incoherent power summation, in which the phase term is not included. Thus, γ_{incoh} does not change with the increasing area. Since all the nine patches are close to the specular point, and the incoherence is less sensitive to the change of slope as shown in Fig. 4, γ_{incoh} stays constant 24 dB, which is the peak value.

We next illustrate the histogram of the phase of the scattered waves. Since AKS is purely analytical for both random roughness of f_1 and f_2, it cannot be used to study the statistics of the phase using
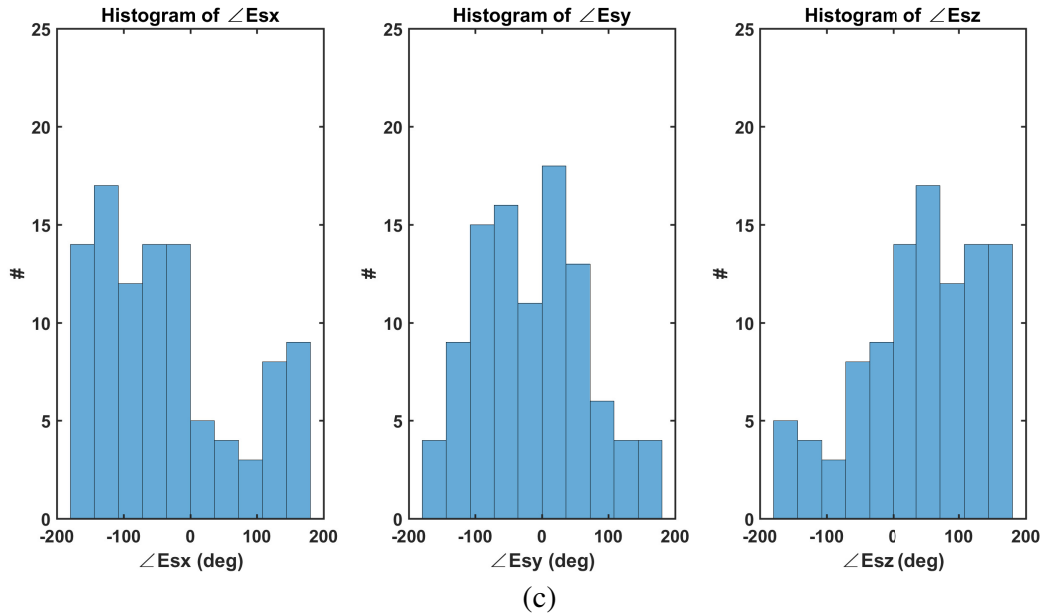

(a)

(b)
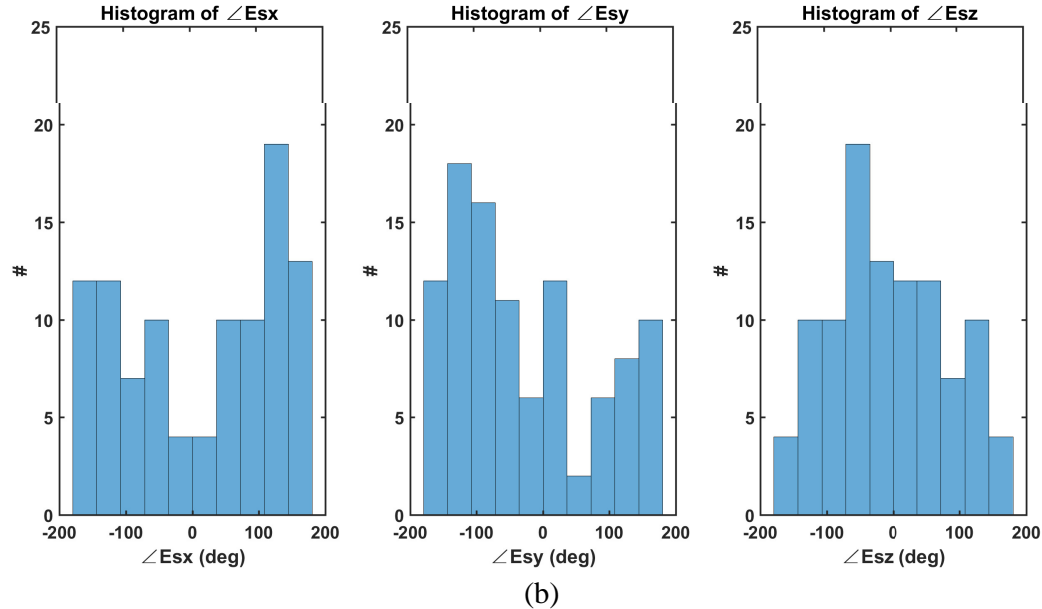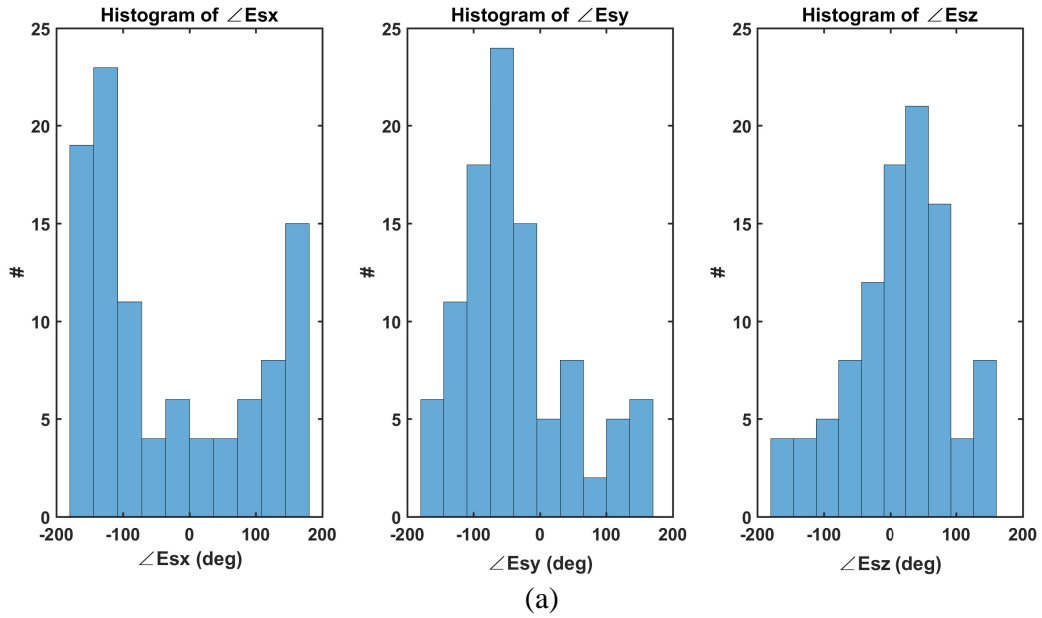
Figure 8. Coherent phase histogram with increasing area size for L band. $h_1 = 1.0$ cm, $h_2 = 4.5$ cm, $l_1 = 10$ cm, $l_2 = 3$ m. (a) $L = 30$ m, (b) $L = 60$ m, (c) $L = 90$ m.

Figure 9. Patch slopes p_{3n} and q_{3n} (in degree) and the DEM heights z_n (in cm) of the 9 DEM patch. γ_{coh} increases with area. The shape of each DEM patch is square with size $\sqrt{A} = 30$ m in simulation.

histograms. However, either NKA or FPCP can be used. Since the results of FPCP are in good agreement with NKA, we can use FPCP for Monte Carlo simulations of the phase of the electric field at L band. The results are shown in Fig. 8. The Monte Carlo simulations are from the realization of $f_2(x, y)$. Figs. 8(a) to 8(c) are corresponding to $\sqrt{A} = 30$ m, 60 m, 90 m. There is a definite phase at $\sqrt{A} = 30$ m. The reason is that, for a single patch, the scattered fields are in phase, which causes a high coherence and a definite phase. As we increase $\sqrt{A}$ to 60 m and 90 m, the phase histogram becomes more uniform. Similar to the previous discussion, when more patches are included, the scattered fields from different patches are not in phase, which decreases the coherence and the phase concentration. In Section 9, we will show the results that are more coherent.

Next, we show a set of results in which γ_{coh} increases with the area. The slopes and DEM heights are shown in Fig. 9, and the results of γ are shown in Fig. 10. As is shown, this region is relatively flat
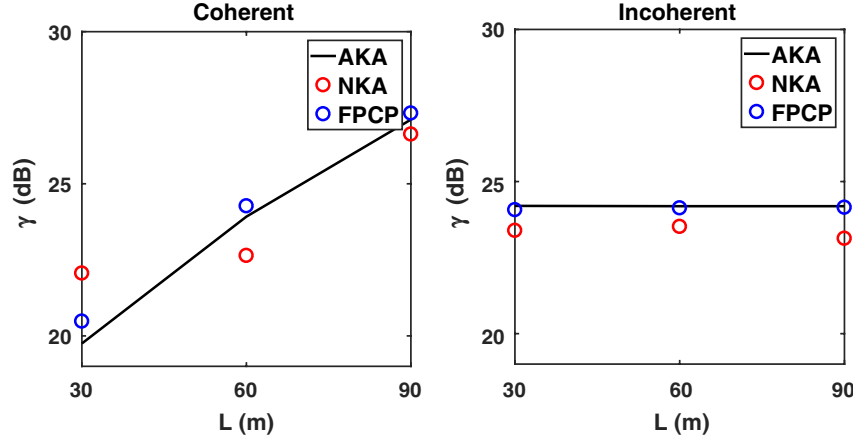
Figure 10. Bistatic scattering coefficients γ for a 30 m DEM patch with increasing area size at L band. γ_{coh} increases with area. $h_1 = 1.0\,\text{cm}$, $h_2 = 4.5\,\text{cm}$, $l_1 = 10\,\text{cm}$, $l_2 = 3\,\text{m}$.

without large slope nor DEM fluctuation. Thus, the fields from different patches are more in-phase. As a result, the coherent fields increase with the area because of the increasing coherent power. The incoherence is still constant with the increasing area.

8.3. Comparisons of AKS Incoherence Waves with GO and GO with Attenuation

Since GO only has incoherent waves, we compare the incoherent waves, γ_{incoh}, of AKS with GO and GO with attenuation (GO-Att). GO-Att is called "improved GO" in Reference [14]. We list typical values of the attenuation factor $\exp(-4k^2 h_1^2 \cos^2 \theta_i)$ in Table 3 with $k = 33\,\text{m}^{-1}$ and $\theta_i = 40°$.

We show the results of incoherence from AKS and GO models. In Fig. 11, we use the roughness parameters as stated previously. In Fig. 12, we use different parameters as shown below:

$$h_1 = 1.5\,\text{cm}, \quad l_1 = 10\,\text{cm}$$
$$h_2 = 4.5\,\text{cm}, \quad l_2 = 3\,\text{m}$$

At the specular angle $\theta_s = 40°$, there is a difference of 1.1 dB between GO and GO-Att in Fig. 11,

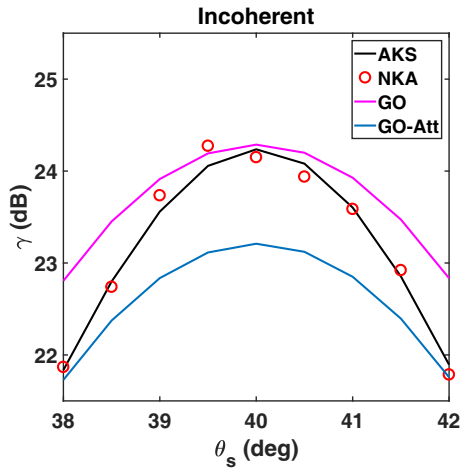**Figure 11.** Bistatic scattering coefficients γ for a 30 m DEM patch with scattering angle θ_s at L band. $h_1 = 1.0\,\text{cm}$, $h_2 = 4.5\,\text{cm}$, $l_1 = 10\,\text{cm}$, $l_2 = 3\,\text{m}$.
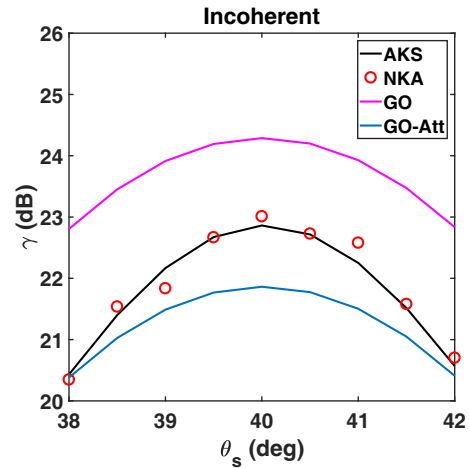
Figure 12. Bistatic scattering coefficients γ for a 30 m DEM patch with scattering angle θ_s at L band. $h_1 = 1.5\,\text{cm}$, $h_2 = 4.5\,\text{cm}$, $l_1 = 10\,\text{cm}$, $l_2 = 3\,\text{m}$.

and a difference of 2.5 dB between GO and GO-Att in Fig. 12. For both cases, the NKA and AKS results fall between GO and GO-Att. Since GO and GO-Att are approximations of the Kirchhoff integral (NKA) as mentioned above, the results in Fig. 11 and Fig. 12 show that GO and GO-Att are less accurate than NKA. The reasons can be analysed as following: (i) since GO does not include the contribution of the microwave roughness f_1, (ii) GO-Att does not include the diffuse incoherent scattering of f_1, (iii) they are different with each other and not agree with NKA. Thus, results from two GO models are not accurate.

An additional result is shown in Fig. 13, in which we are using the parameters as shown below:

$$h_1 = 3.5\,\text{cm}, \quad l_1 = 14\,\text{cm}$$
$$h_2 = 4.0\,\text{cm}, \quad l_2 = 2\,\text{m}$$

In this case, there is only 0.5 cm difference between h_1 and h_2, which means the dividing line between f_1 and f_2 is not clear. Since GO model requires dividing line between microwave scale and fine scale, it is difficult for GO to be implemented for this case. However, AKS is still valid because the dividing line is not needed. For this case, there is more than 10 dB difference between GO and GO-Att.
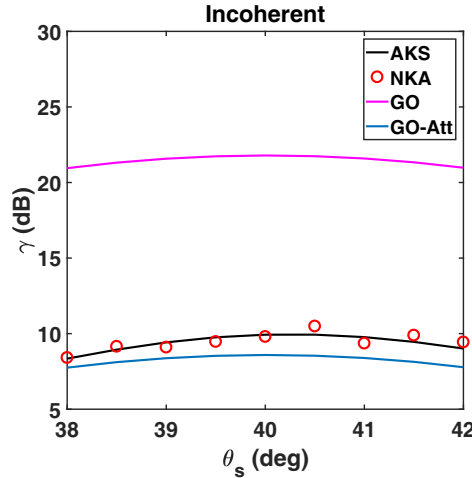

Figure 13. Bistatic scattering coefficients γ for a 30 m DEM patch with scattering angle θ_s at L band. $h_1 = 3.5\,\text{cm}$, $h_2 = 4.0\,\text{cm}$, $l_1 = 14\,\text{cm}$, $l_2 = 2\,\text{m}$.

8.4. Cases that $f_{12}(x,y)$ is Non-Separable into $f_1(x,y)$ and $f_2(x,y)$

Next we consider the cases that $f_{12}(x,y)$ is non-separable into $f_1(x,y)$ and $f_2(x,y)$. In case a, we use the usual case $f_1 + f_2$ as previously described. The surface parameters are shown below:

$$h_1 = 2.0\,\text{cm}, \quad l_1 = 14\,\text{cm}$$
$$h_2 = 6.0\,\text{cm}, \quad l_2 = 5.4\,\text{m}$$

In case b, we have a correlation function $C(\rho)$ graphically specified as shown in Fig. 14(a). For this case, the rms height for the surface is $h = 6.32$ cm. There is no correlation length as defined by Gaussian nor exponential. Here we use $C(\rho) = 1/e$, then $l = 2.78$ m. In case c, we have a surface spectrum graphically specified as shown in Fig. 14(b). Based on Eq. (4) and Eq. (5), $h = 6.75$ cm and $l = 4.60$ m. Note that the $W(k)$ of case c is not the Fourier transform of $C(\rho)$ of case b. In Fig. 14(c), h and $C(\rho)$ for the three cases are illustrated by plotting $\exp[-k_{dz}^2 h^2 (1 - C(\rho))]$ as a function of ρ. The results for separate f_1 and f_2 are also included. The values of ρ are truncated when the the exponential values fall to 0.01.

For cases b and c, the GO models cannot be applied, because GO depends on the separation into f_1 and f_2. However, the AKS, FPCP, and NKA can be applied. The results of γ are shown in Fig. 15. As is shown, the γ results are obtained for cases b and c using AKS.
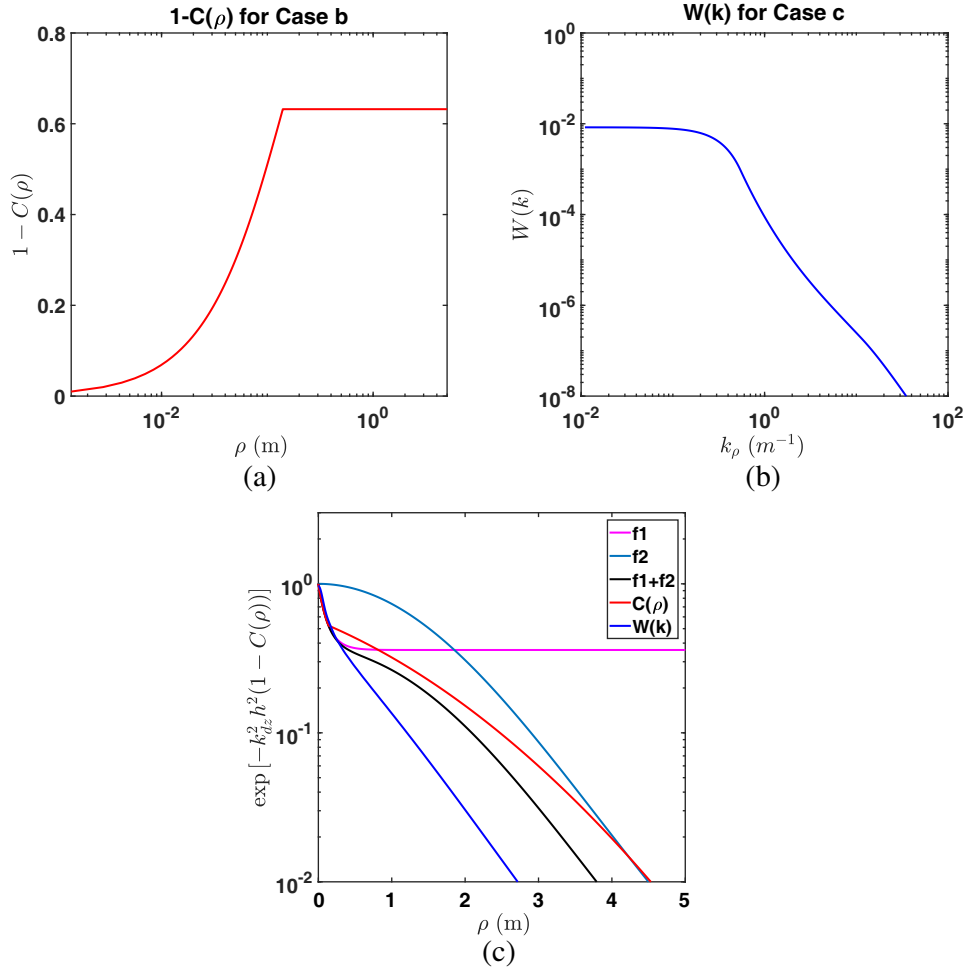
Figure 14. Surface correlation function and spectrum for $f_1 + f_2$, random correlation function $C(\rho)$, and random spectrum $W(k)$. For f_1 and f_2, $h_1 = 2.0\,\text{cm}$, $h_2 = 6.0\,\text{cm}$, $l_1 = 14\,\text{cm}$, $l_2 = 5.4\,\text{m}$. (a) Random $C(\rho)$ for case b. (b) Random $W(k)$ for case c. (c) Plots of $\exp[-k_{dz}^2 h^2(1 - C(\rho))]$ for three cases.

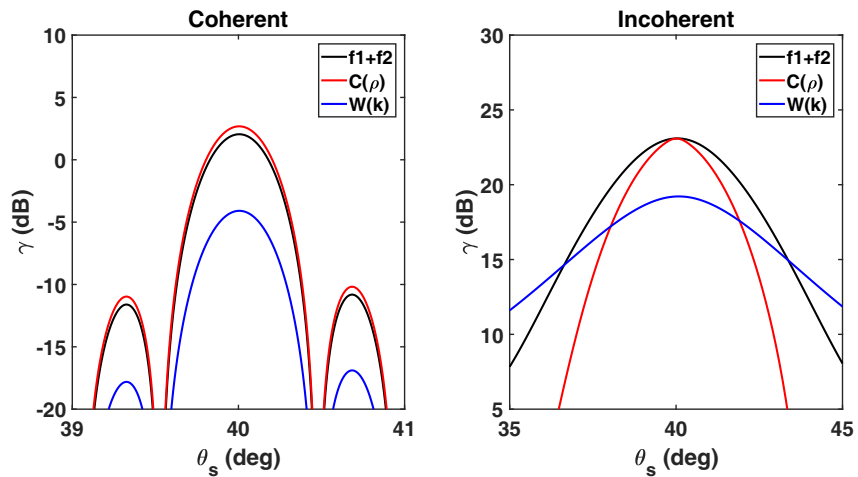**Figure 15.** Bistatic scattering coefficients γ for $f_1 + f_2$, random correlation function $C(\rho)$, and random spectrum $W(k)$. For f_1 and f_2, $h_1 = 2.0\,\text{cm}$, $h_2 = 6.0\,\text{cm}$, $l_1 = 14\,\text{cm}$, $l_2 = 5.4\,\text{m}$.

8.5. Delay-Doppler Map (DDM)

Next we compare DDM. The track wise comparison is performed with CYGNSS v3.0 data from Physical Oceanography Distributed Active Archive Center (PODAAC). We use the track data collected near the Z1 cal/val site $(37°11'26.26''N, 105°59'31.64''W)$ in San Luis Valley, CO, USA. The data is collected on

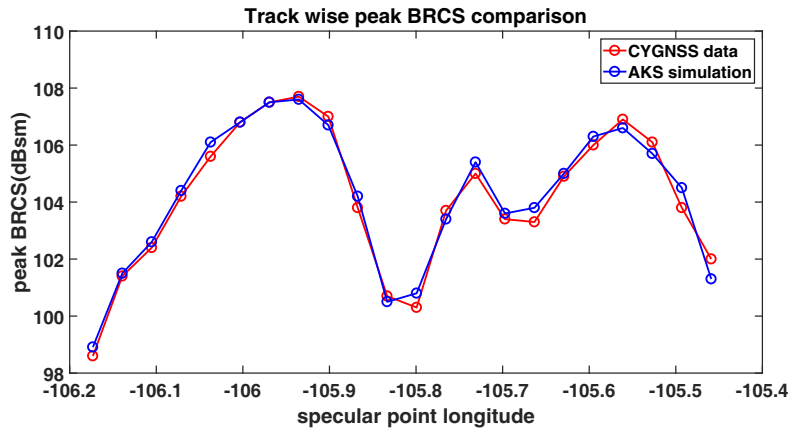**Figure 16.** Track wise peak BRCS comparison. $h_1 = 1\,\text{cm}$, $h_2 = 5\,\text{cm}$, $l_1 = 10\,\text{cm}$, $50h_1 < l_2 < 130h_1$. Variation of l_2 is given in Table 4.

Table 4. l_2 with respect to longitude of specular points along the track.

Longitude (degree)	l_2 (times of h_2)
-106.173	50
-106.139	75
-106.105	75
-106.071	95
-106.037	115
-106.003	115
-105.969	120
-105.935	130
-105.901	130
-105.867	100
-105.833	60
-105.799	50
-105.765	75
-105.731	115
-105.697	75
-105.663	75
-105.629	95
-105.595	120
-105.561	130
-105.527	130
-105.493	130
-105.459	75

day 301 of 2019 by craft 02 in channel 3. The time index is from 101225 to 101246. The specular points of the track of data we pick starts from (37.1817°N, 106.1732°W), and ends at (37.2451°N, 105.4590°W).

In Fig. 16, a track wise comparison for the peak value bistatic radar cross section (BRCS) between CYGNSS data and AKS is shown. The soil permittivity is selected as $\varepsilon = 3.293 + 0.198i$ based on the ground soil moisture measurement. We keep $h_1 = 1$ cm, $h_2 = 5$ cm, $l_1 = 10$ cm, and change the l_2 between $50h_1$ to $130h_1$ for mountainous and plain area respectively. In Table 4, we show the values of l_2 along the track. The difference between this comparison and the comparison in [15], is that the l_2 is fixed at $130h_2$ in [15], while l_2 is a variable in this paper as shown in Table 4.

The size of the area that contributes to the Delay-Doppler along the track is $45000\,\mathrm{km}^2$. The p_{3n} and q_{3n} of the 30 m patches are derived from DEM over this area. As is shown in Fig. 16, the simulation results of AKS are in good agreement with the data for the entire track. The differences are less than 0.5 dB.

9. RESULTS FOR P BAND: COHERENT AND INCOHERENT WAVES

In this section, we show the results for P band ($freq = 370\,\mathrm{MHz}$). There are interests in using the coherent waves of P band, because with longer wavelength than L band, the coherent waves at P band can be strong even for large areas. The height of the transmitter and receiver are 35900 km and 500 km, respectively. The incident angle is $\theta_i = 40°$. For P band, we use the actual land surface elevation from DEM. That is, for each DEM patch, the elevation z_{3n} and the slopes p_{3n} and q_{3n} of the patch are retrieved from the SRTM data. The DEM patch resolution for the data is 30 m, which is the same as that for L band. Three DEM profiles are selected from the areas of Colorado. The three areas are named as Sanford, Brazos Peak, and Lobato Tank. The geographic information of these three profiles is shown in Table 5. The elevation differences are ranging from low to high, and are quantified by the rms of the DEM. Since the wavelength of P band is less than 1 m, the microwave roughness f_1 with $h_1 = 1$ cm is ignored. The rms and correlation length of f_2 are assumed to be $h_2 = 4.5$ cm and $l_2 = 3.0$ m. These specifications are kept for all following except stated otherwise.

Table 5. Geographic information of three sites from Colorado.

Site	rms of DEM (m)	Lon (deg)	Lat (deg)
Sanford	1.76	-105.908	37.294
Brazos Peak	16.83	-106.375	36.825
Lobato Tank	31.67	-106.270	36.930

9.1. Phase Histogram to Illustrate the Coherence

We first discuss the phase histogram of the scattered fields at P band, since a promising application for P band is snow depth remote sensing based on phase measurements. The area of the land surface is $600\,\mathrm{m} \times 600\,\mathrm{m}$, and the area center is located at the specular point. The observing direction is along the specular direction, which means $\theta_s = \theta_i = 40°$. We implement NKA to calculate the histogram of the phase based on Monte Carlo simulations with 50 realizations of f_2. The results of γ are shown in the next subsection, in which we will discuss the changes of coherence and incoherence with the rms height of DEM.

The surface profiles and phase histogram of the scattered fields are shown in Figs. 17 to 19. In Fig. 17, the results for DEM with low elevation differences are illustrated, of which the rms is 1.76 m. In Fig. 17(a), we show the relative elevations of the area at latitude and longitude of the first place. This area is at a plain, with small elevation variations. The histogram of the phases is shown in Fig. 17(b). There is definitely a specific phase, which means that the coherence dominates in the total scattered fields. This is also verified by the γ values shown in Table 6 in next subsection, as γ_{coh} is 15 dB higher than γ_{incoh}.
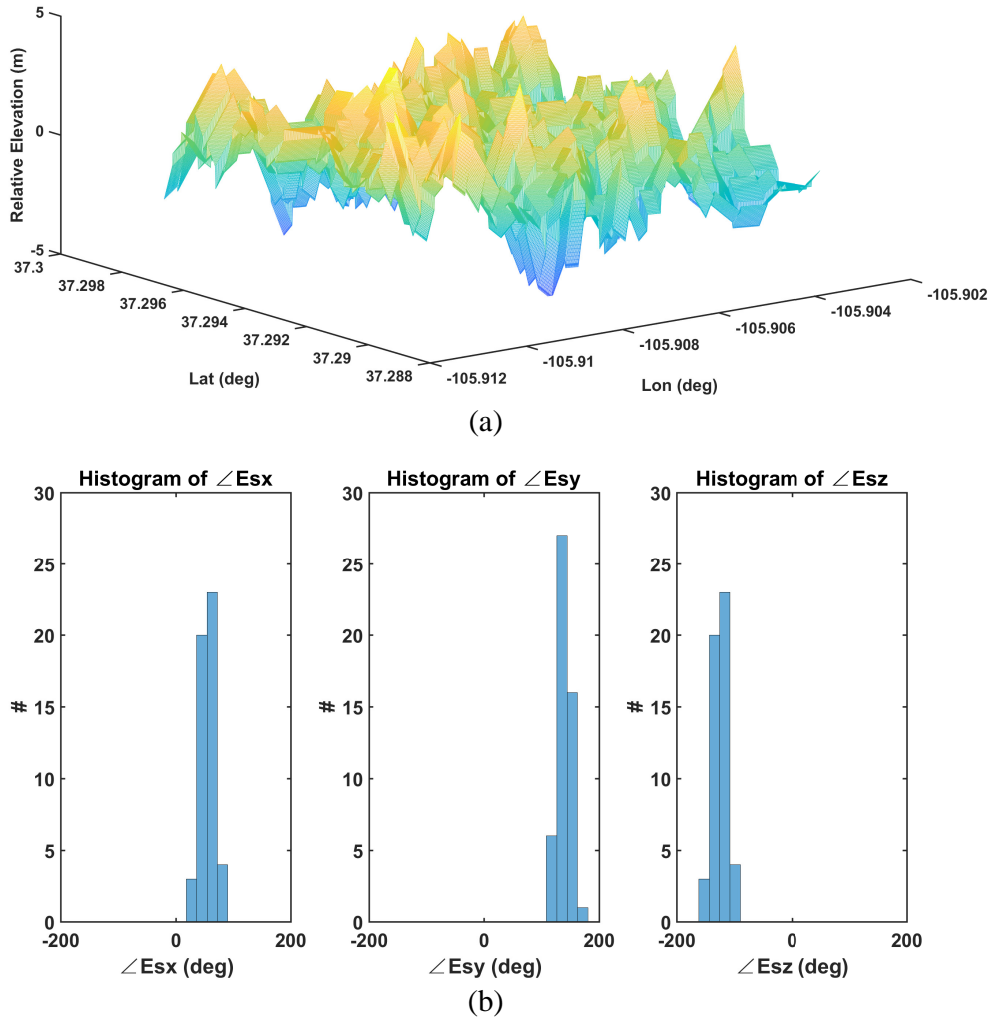
Figure 17. Phase histogram at P band with low elevation differences at Sanford $(105.908°\text{W}, 37.294°\text{N})$. $h_2 = 4.5\,\text{cm}$, $l_2 = 3\,\text{m}$, rms of DEM is $1.76\,\text{m}$. (a) Profile of the land surface at Sanford. (b) Phase histogram.

Similar to the discussion for L band, the positions and scattered angles of each DEM patch do not have a significant impact on the decrease of the coherence, as all patches are around the specular point, and also close to each other. In addition, the scattered directions are all around the specular direction. The most significant factors are the effects of elevations and slopes on the phase terms. For the first case with low rms height, the area is flat and horizontal, which means the slopes of all DEM patches are relatively small. Since the wavelength $\lambda = 0.81\,\text{m}$, which is comparable to the rms of DEM, the change of the total distance of the waves in the phase term $\exp[ik(R_{nt} + R_{nr})]$ would be small. As a result, the scattered fields from most DEM patches can be regarded as in-phase waves, which leads to a high concentration of the phase.

In Fig. 18, we consider the case of moderate elevation for which the rms height of DEM is $16.83\,\text{m}$. Fig. 18(a) shows the relative elevation of Brazos Peak at Colorado. In Fig. 18(b), the phase distribution becomes slightly more uniform compared with the case of Fig. 17(b). However, the phase concentration is still clear. In this case, h_3 is larger than the wavelength of P band, which leads to a higher fluctuation of patch slopes and scattered phase from patch to patch. As a result, most of the scattered fields are not in phase. The coherent fields can cancel each other and lead to a relatively uniform phase distribution. However, since the coherence dominates, the phase of the scattered fields still shows a maximum.

In Fig. 19, we consider the case corresponding to large DEM rms height of $31.67\,\text{m}$, which is much
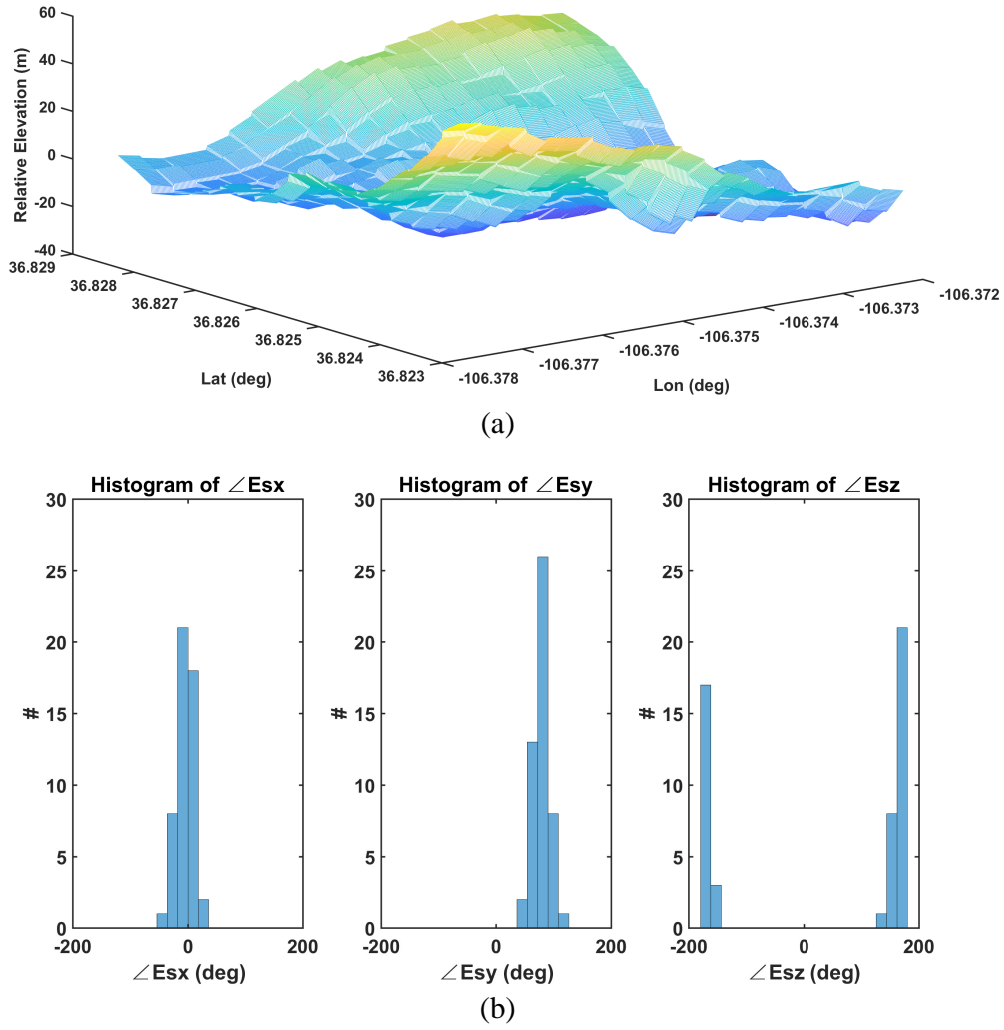
(a)

(b)

Figure 18. Phase histogram at P band with medium elevation differences at Brazos Peak (106.375°W, 36.825°N). $h_2 = 4.5$ cm, $l_2 = 3$ m, rms of DEM is 16.83 m. (a) Profile of the land surface at Brazos peak. (b) Phase histogram.

larger than the P band wavelength, as shown in Fig. 19. From Fig. 19(a), we notice that the entire area has a tilted slope. Both coherent fields and incoherent fields are much weaker due to the shifted local specular direction. In this case, the elevation difference is high that the slopes and phase terms of different patches are varying significantly. Also, the significant slope means that all patches are tilted towards a direction other than the specular direction. As a result, the total received fields are weak, and the phase histogram is much more uniform. However, the scattered fields still concentrate around a certain phase due to the slightly dominance of the coherence as shown in Table 6. As an explanation, although the total area is obviously tilted, there always exists some regions locally horizontal within this area. These regions provide contributions to the in-phase fields in the observing direction, which leads to a phase concentration, and shows the feasibility of phase measurements.

As a conclusion, at P band, the phase measurements are valid for both low and high elevation differences. For low elevation differences, the area is relatively flat and horizontal, for which the phase of the scattered fields has a definite concentration. For high elevation differences, or even larger tilted angle, the distribution of the phase can be more flat. However, there would be some locally horizontal regions in the total area, which contribute a relatively higher phase concentration in the observing direction.
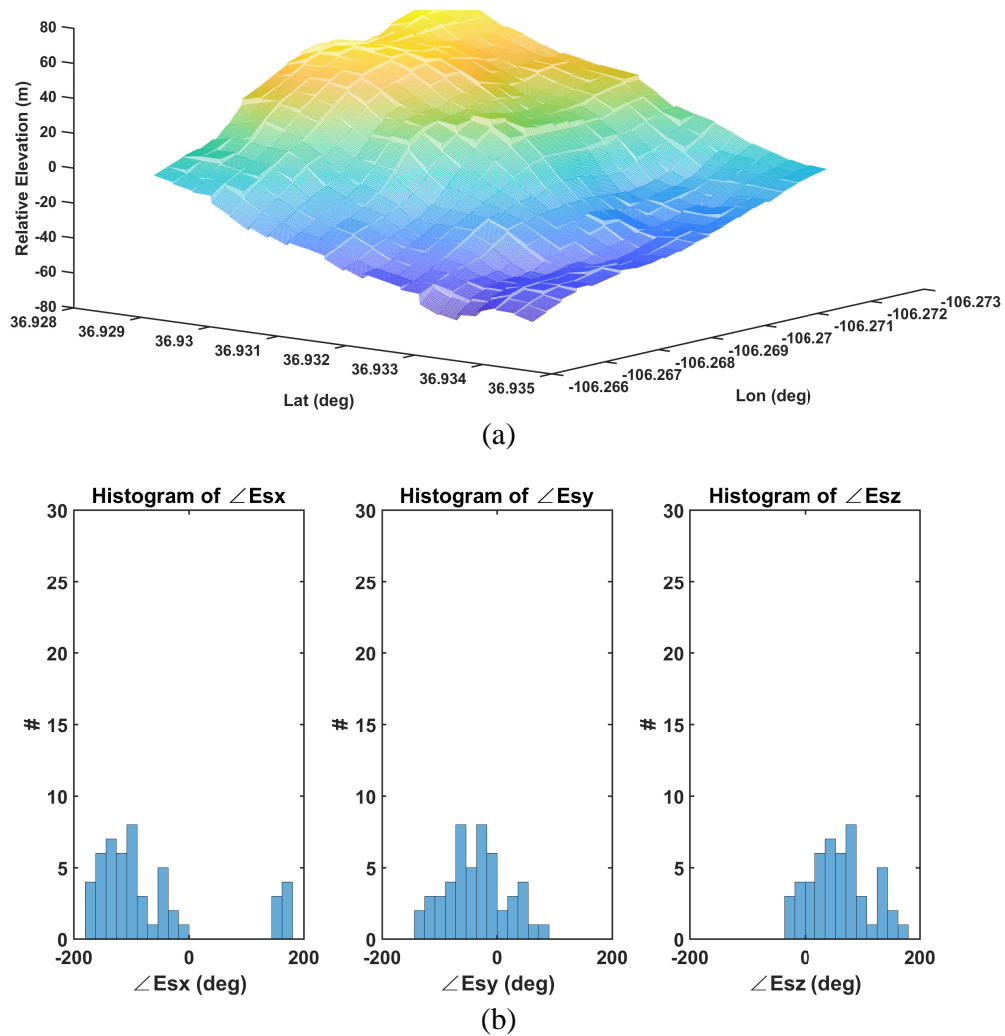
(a)

(b)

Figure 19. Phase histogram at P band with high elevation differences at Lobato Tank (106.270°W, 36.930°N). $h_2 = 4.5\,\mathrm{cm}$, $l_2 = 3\,\mathrm{m}$, rms of DEM is $31.67\,\mathrm{m}$. (a) Profile of the land surface at Lobato Tank. (b) Phase histogram.

Table 6. Bistatic scattering coefficients of three sites from Colorado.

Site	rms of DEM (m)	γ_{coh} (dB)	γ_{incoh} (dB)
Sanford	1.76	24.42	9.70
Brazos Peak	16.83	3.71	-0.92
Lobato Tank	31.67	2.35	0.66

9.2. Coherent Fields and Incoherent Fields with the Changes of the RMS Height of DEM

Next the bistatic scattering coefficients γ with the changes of the rms height of DEM are discussed. The same simulation parameters and DEM profiles as Section 9.1 are applied. However, we calculate γ_{coh} and γ_{incoh} using AKS, since AKS provides the analytical results of coherence and incoherence. The results of γ are shown in Table 6. As is shown, both γ_{coh} and γ_{incoh} are decreasing with the increasing rms height of DEM. As discussed before, higher rms of DEM implies higher elevations and slopes fluctuations, or tilted angle. For the first site, the rms of DEM is low. As is shown in the profile of the land surface, this site is relatively flat and horizontal. In this case, a large part of the scattered

power is transmitted to the observing direction, which leads to both high γ_{coh} and γ_{incoh}.

When considering higher rms of DEM, the second site Brazos Peak as an example, the scattered power in the observing direction is lower. Since the ratio of horizontal region, which contributes more coherence, is lower for high rms area, the γ_{coh} is much lower than the first case. In addition, we noticed that γ_{incoh} is also smaller. From Eq. (93), we have discussed that the term $\sqrt{(k_{dxn} + k_{dzn}p_{3n})^2 + (k_{dyn} + k_{dzn}q_{3n})^2}$ contributes to the oscillation of the Bessel function. For the area with large slope, the values of p_{3n} and q_{3n} can be large, which increases the oscillation of J_0 in the integrand and decrease the integral of $D_{I_n}^{(N)}$. As a result, the incoherence bistatic scattering coefficients would be reduced.

For the third case, in which the total area is obviously tilted, we can imagine that the most scattered power is not transmitted to the observing direction. As a result, both γ_{coh} and γ_{incoh} are weak comparing with the two previous cases.

9.3. Coherent Fields and Incoherent Fields as a Function of the Area Size up to 1.5 km

In this subsection, we examine the changes of the coherent wave and incoherent wave with respect to the area size $L = \sqrt{A}$. Here, we fix the observing direction at $\theta_s = 40°$, and increase the area size from $L = 600\,\text{m}$. The center of the area of each size is located at the specular point $(0, 0, 0)$. Three cases are considered. In the first case, the position from Sanford is selected for simulation, which is the most flat area. As is shown in Fig. 20, the results are similar to that of L band. That is, the coherence decreases with the increasing area size, while the incoherence remains relatively constant. When the area size is as large as $L = 1500\,\text{m}$, the coherence is low that the incoherence dominates. In this case, waves are still coherent for much larger areas than L band. As discussed in the previous case, in the specular direction ($\theta_s = 40°$), the coherence dominates due to the relatively flat and horizontal area. Since the phase term from the increasing number of DEM patches can lead to the scattered fields not being in phase, the total coherent fields decrease with the area size.

In the first case, the area from Sanford is relatively flat with small rms height of DEM. As a result, the coherent waves can be much stronger than incoherence for 1 km or 2 km. In some other cases, the coherence can be comparable, or even less than incoherence. In the second case, we implement the same simulation over the DEM profile from Lobato Tank, which is tilted as shown in Fig. 19(a). The results of γ are shown in Fig 21. In this case, the γ_{coh} and γ_{incoh} are comparable for $L = 600\,\text{m}$. When L is increased to 750 m and 900 m, γ_{coh} decreases and becomes lower than γ_{incoh}. The results are similar to
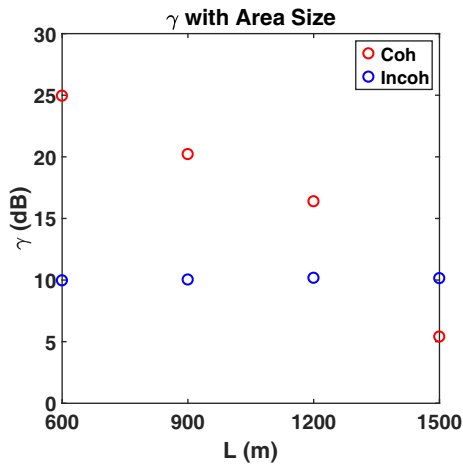

Figure 20. Bistatic scattering coefficients γ with the area size L at Sanford (105.908°W, 37.294°N). The results are from AKS with $h_2 = 4.5\,\text{cm}$, $l_2 = 3\,\text{m}$.
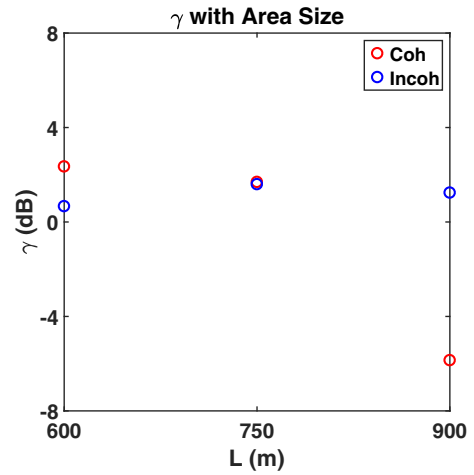
Figure 21. Bistatic scattering coefficients γ with the area size L at Lobato Tank (106.270°W, 36.930°N). The results are from AKS with $h_2 = 4.5\,\text{cm}$, $l_2 = 3\,\text{m}$.

that of L band: for areas with large slope and elevation fluctuations, the coherence would decrease with increasing area size, and incoherence would dominate in the end.

Finally, we examine a third case where the DEM is from Brazos Peak. The simulation results are shown in Fig. 22. As is shown, the γ_{coh} is much larger than γ_{incoh}, which means the coherence dominates. In addition, γ_{coh} increases with the increasing area size L. We show that the coherent can also increase with the area size for some cases.
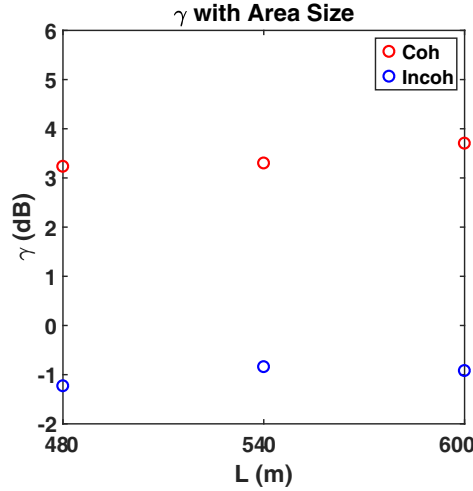

Figure 22. Bistatic scattering coefficients γ with the area size L at Brazos Peak ($106.375°$W, $36.825°$N). The results are from AKS with $h_2 = 4.5$ cm, $l_2 = 3$ m.

In examples given above, the coherence of signals at P band has been shown. In real remote sensing applications, the phase is measured for snow mass retrieval [11] and the reflectivity is measured for soil moisture retrieval [22].

10. COMPUTATIONAL STEPS AND CPU COMPARISONS

In this section we describe the computational steps for AKS and the CPU comparisons of three methods: NKA, AKS, and GO without attenuation. Since GO model gives the incoherent waves, only the computational steps and CPU of the incoherent wave are considered. The area is one 15 km by 15 km DDM pixel. The GO method is the fastest and has been adopted by numerous investigators following the work by Zavorotny and Voronovich [13]. By GO in this section, we mean GO without attenuation. As explained below, we have optimized the computation of AKS, so that the CPU of AKS is only slightly more than that of GO.

Unless specified, we are using the following surface parameters:

$$h_1 = 1.0\,\mathrm{cm}, \quad l_1 = 10\,\mathrm{cm}$$
$$h_2 = 5.0\,\mathrm{cm}, \quad l_2 = 5\,\mathrm{cm}$$

We first consider AKS on a single 30-meter DEM patch. Since the observation direction is in the vicinity of the specular direction, we let $k_{dzn} = -2k\cos\theta_i$, $k_{dzn}^2 = 4k^2\cos^2\theta_i$, which are constants.

As shown in Section 2, the incoherent intensity equations of AKS are Eq. (6), Eq. (40), and Eq. (47) as shown below:

$$h^2 C(\rho) = 2\pi \int_0^{k_{\rho,\max}} dk_\rho k_\rho W\left(k_\rho\right) J_0\left(k_\rho\rho\right)$$

$$D_{I_n}^{(N)} = 2\pi k^2 \int_0^{\rho_{\max}} d\rho \rho J_0\left(\alpha\rho\right)\left\{\exp\left[-k_{dzn}^2 h^2\left(1 - C(\rho)\right)\right] - \exp\left(-k_{dzn}^2 h^2\right)\right\} \qquad (97)$$

$$\gamma_{n,\,\text{incoh}} = \frac{\cos\theta_i}{\pi}\left[\frac{|R_v(\theta_{in})|^2 + |R_h(\theta_{in})|^2}{2}\right]D_{I_n}^{(N)}$$

Note that

$$\exp\left[-k_{dzn}^2 h^2\left(1 - C(\rho)\right)\right] = \exp\left[-k_{dzn}^2 h_1^2\left(1 - C_1(\rho)\right) - k_{dzn}^2 h_2^2\left(1 - C_2(\rho)\right)\right]$$

Even if $k_{dzn}^2 h_2^2$ can be large, $(1 - C_2(\rho))$ can be small, which makes the integral well-behaved. We treat $h^2 C(\rho)$ as combined $f_{12}(x, y)$. For the case that decomposition is possible with

$$f_{12}(x, y) = f_1(x, y) + f_2(x, y)$$

we have:

$$h^2 C(\rho) = h_1^2 C_1(\rho) + h_2^2 C_2(\rho)$$

In the equation above, α is a variable of the slopes and positions of the 30-meter DEM patch:

$$\alpha = \sqrt{\left(k_{dxn} + k_{dzn}p_{3n}\right)^2 + \left(k_{dyn} + k_{dzn}q_{3n}\right)^2}$$

We label the steps that are not repeated for every 30-meter patch as "set-up". The calculation of Eq. (95) is labelled as a set-up step. For one choice of $W(k_\rho)$ or $h^2 C(\rho)$, $D_{I_n}^{(N)}$ is only a function of α. We generate a look-up table for $D_{I_n}^{(N)}$ as a function of the variable α. The CPU is 0.49 seconds. If several choices are needed for the $15\,\text{km} \times 15\,\text{km}$ DDM, then the CPU is 0.49 seconds multiplied by number of choices. Even with 100 choices, the CPU is only 49 s.

The steps of set-up for AKS are as following:

(1) Calculate the rms height h and the correlation function $C(\rho)$ from the surface spectrum $W(k_\rho)$. Notice that h can be obtained by making $\rho = 0$ in the integral of Eq. (6).

(2) Calculate $D_{I_n}^{(N)}$ for a single specific value of α using the calculated $C(\rho)$.

The numerical parameters for step (1) and (2) are selected as following:

$$k_{\rho,\text{max}} = 3k = 99$$
$$\rho_{\text{max}} = 2l_2 = 10$$
$$dk_\rho = 0.66$$
$$d\rho = 1l_1 = 0.1$$
$$N_{k_\rho} = \frac{k_{\rho,\text{max}}}{dk_\rho} = 3000$$
$$N_\rho = \frac{\rho_{\text{max}}}{d\rho} = 100$$

(3) Change the value of α and generate several values of $D_{I_n}^{(N)}$. Then interpolate the calculated $D_{I_n}^{(N)}$ to obtain a look-up table. For a DDM area from San Luis Valley of $30\,\text{km} \times 30\,\text{km}$, we calculate the histogram of α values. The histogram is shown in Fig. 23.

As a result, about 99.95% of α are less than 40. Thus, we can select $\alpha_{\text{max}} = 40$ as the upper limit of the look-up table. The numerical parameters of α and the interpolation discretization $d\alpha_{\text{interp}}$ are shown as follows:

$$\alpha = 40$$
$$d\alpha = 0.1$$
$$d\alpha_{\text{interp}} = 0.05$$
$$N_\alpha = \frac{\alpha_{\text{max}}}{d\alpha} = 400$$
$$N_{\text{interp}} = \frac{\alpha_{\text{max}}}{d\alpha_{\text{interp}}} = 800$$

In this research, we test the CPU time of the three steps. The test results are shown in Table 7. Notice that since step (2) is a part of step (3), the time for step (3) is approximately the time for step (2) multiplied by the number of α selected, which is 400 in this case.
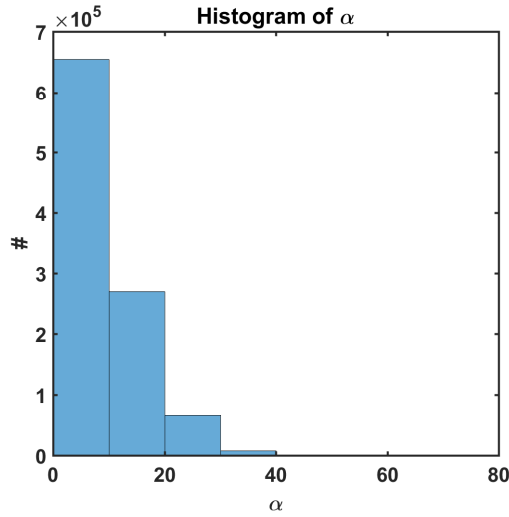
Figure 23. Histogram of α in $D_{I_n}^{(N)}$. The DEM slopes are from San Luis Valley of $30\,\mathrm{km} \times 30\,\mathrm{km}$.

Table 7. Set-up time of the three steps for AKS.

Step	CPU Time
(1)	$0.11\,\mathrm{s}$
(2)	$1\,\mathrm{ms}$
(3)	$0.38\,\mathrm{s}$

As a result, the total time for generating the AKS look-up table for a single $h^2 C(\rho)$ is:

$$0.11 + 0.38 = 0.49\,\mathrm{s}$$

Since we obtain $D_{I_n}^{(N)}$ by searching the look-up table instead of directly implementing the integration, the computation is fast. For each 30-meter DEM patch, we obtain the bistatic scattering coefficients γ_{incoh} using Eq. (47) and the look-up table of $D_{I_n}^{(N)}$.

For GO, the set-up step is the calculation of h_1 and slope $h_2 = l_2$ from the surface spectrum. According to the test results, the set-up time for GO is $0.23\,\mathrm{s}$. Since NKA can be implemented on the surface heights from lidar measurements directly, there is no set-up step for NKA.

The CPU times for the three methods are shown in Table 8. The CPU time test is implemented on a ThinkPad laptop with an Intel Core i7-5500 processor of $2.40\,\mathrm{GHz}$. For a fair comparison, only one single CPU core is used. In the first two rows, three methods and their corresponding discretization are listed. The set-up time is shown in the third row. As is shown, the set-up is only applied to AKS, and the CPU time is $0.49\,\mathrm{s}$. In the next row, the CPU time for retrieving DEM slope p_{3n} and q_{3n} from the SRTM data is shown. Since all the three methods are using the same definition of DEM slopes, the CPU time are the same. In the fifth row, the CPU time for a single 30-meter DEM patch is shown. In this case, CPU time is for one calculation without the time for slope computation. Specifically, it means the time for NKA with only one realization, and the time for AKS using the calculated $D_{I_n}^{(N)}$ look-up table. For GO, it means the time for a single DEM patch. In the sixth row, the total time for slopes and γ_{incoh} are shown, which is the time to obtain the final results of γ_{incoh} on a single 30-meter DEM patch. That is, this time is the summation of that in the fourth and fifth row. In the seventh row, the CPU time for a single DDM pixel computation without including the set-up time is shown. In our test, the size of the DDM area is $15\,\mathrm{km} \times 15\,\mathrm{km}$, which means the total number of 30-meter DEM patches on a single DDM pixel is:

$$(15\,\mathrm{km}/30\,\mathrm{m})^2 = 250000$$

Table 8. CPU time comparisons for NKA, AKS, and GO.

CPU based on a single core	NKA	AKS	GO
Discretization	2 cm	30-meter DEM patch	30-meter DEM patch
One time set-up (steps that are not repeated for every 30-meter patch)	None	0.49 s (Integral over $W(k)$ and look-up table for $D_{I_n}^{(N)}$ once each time)	0.23 s (Integral over $W(k)$ for calculation of h_1 and s_2 from spectrum of f_1 and f_2)
30-meter patch, computing p_{3n} and q_{3n}	0.01 ms	0.01 ms	0.01 ms
30-meter γ_{incoh} computation	2.49 min	0.09 ms	0.07 ms
CPU for 30 m patch (total time for computing p_{3n}, q_{3n}, and γ_{incoh})	2.49 min	0.10 ms	0.08 ms
CPU for 15 km DDM pixel Not including set-up	2970 h (projected time for 15 km DDM according to Table 3 in [19])	25 s	20 s
CPU for 15 km DDM pixel Including set-up	2970 h (projected time for 15 km DDM according to Table 3 in [19])	25.49 s	20.23 s

Table 9. CPU time for NKA examples in this paper.

CPU for NKA Examples in This Paper	30 m Area	60 m Area	90 m Area
One realization Without acceleration	2.49 min	9.87 min	22.44 min
One realization With Matlab matrix acceleration	3.24 s	13.11 s	28.87 s
50 realizations With Matlab matrix acceleration	2.70 min	10.93 min	24.06 min

Thus, the CPU time for AKS and GO in this row is that in the sixth row multiplied by 250000. For NKA, the computation is time consuming for such large area. Thus, we refer to the test results from Table 3 in the Reference [19]. In that case, 10 km × 10 km DDM area was considered, and the CPU time for one single realization with 33 CPU cores is 40 hours. Thus, under the same conditions, the CPU time for 15 km × 15 km DDM area with one core and one realization should be:

$$40 \, \text{h} \times 33 \times (15 \, \text{km}/10 \, \text{km})^2 = 2970 \, \text{h}$$

In the last row, the CPU time for a single DDM pixel computation including the set-up time is shown. Since there is no set-up for NKA and GO, the time is the same as that in the seventh row. For AKS, the time is the summation of that in the third and seventh row.

As is shown, NKA is time consuming because of 2 cm discretization. The CPU time for AKS and GO are quite close with AKS requiring slightly more CPU. In implementation of NKA, realizations need to be taken and calculations are performed on high performance computers. Thus, using 33 cores

as reported in [19], the CPU time was 40 hours for 10 km DDM. If 1000 cores are applied, then the projected CPU is 1.3 hours.

Next we give the CPU for NKA examples in this paper, as shown in Table 9. NKA approach is important because it provides accurate benchmark solution for brute force integration for the vector Kirchhoff integral. Also it provides histograms of amplitude and phase so that statistics of amplitude and phase fluctuations can be derived. In using NKA for validation of AKS, as shown in Fig. 7, the areas are 30 m × 30 m, 60 m × 60 m, and 90 m × 90 m. In this table, the time for NKA with one realization is different from that in Reference [19], and the time in this table is the real tested time in the examples of this paper. As is shown, the CPU times without acceleration and with Matlab matrix acceleration are listed. Since NKA implements the similar operation for each of the 2 cm patches, the matrix operation are applied in the real tests for multiple realizations to shorten the computation time.

11. CONCLUSION

Reflections near specular direction are strongly affected by topography unlike radar backscattering and passive emissivity. Signals have more heterogeneous spatial variations from rough/topography surface scattering. However, topography is time constant and the bias effects can be incorporated in physical models as shown in this paper. In Signals of Opportunities at P band and L band, bistatic scattering are measured in the vicinity of the specular direction. Although vector Kirchhoff integral is not accurate for radar backscattering, it is quite accurate in the vicinity of the specular direction as verified by full wave simulations of Maxwell equations [21, 23]. We have used three Kirchhoff approaches: NKA, FPCP, and AKS. In this paper, the new approach AKS is presented for GNSS-R land applications. The profile of the land surface is assumed to be composed of f_{12} and f_3, in which f_{12} is a combined random roughness, and f_3 consists of deterministic planar patches of DEM. Both coherent and incoherent waves are derived for AKS. In AKS, Monte Carlo simulations and dividing line between microwave roughness and fine scale topography are not required. Since NKA is the benchmark, both AKS and FPCP have been validated by NKA. The results of coherent waves and incoherent waves from AKS, FPCP and NKA are indistinguishable from each other. In comparison with the two versions of GO, with and without microwave attenuation, it is shown that the AKS results fall between the two versions. Results of Cross-Track are also in excellent agreement with CYGNSS data by merely changing l_2. Recently, pattern recognition of satellite data has been used to classify coherence and incoherence [24]. In this paper, we used first principle calculations to derive coherent waves and incoherent waves. The calculations based on physical model also provide a breakdown of the contributions of σ_0. The results in this paper show that patches that have small roughness and topography slope have σ_0 that are more than 10 dB larger than patches that have large roughness and topography slopes. This means that in retrieving soil moisture from GNSS-R reflections [1, 5, 8, 18, 25–27], the contributions of σ_0 can come from a fraction of the pixel rather than uniformly from the entire pixel. At P band, the results of histogram of the phase of the scattered waves show that the coherent waves can still be strong for large area such as 1.5 km. With new SAR technology [28] implemented for Signals of Opportunities, the coherent waves will gain importance for remote sensing land applications. The methodology in this paper can be extended to inland water body and wetlands.

ACKNOWLEDGMENT

REFERENCES

1. Al-Khaldi, M. M., J. T. Johnson, A. J. O'Brien, A. Balenzano, and F. Mattia, "Time-series retrieval of soil moisture using CYGNSS," *IEEE Transactions on Geoscience and Remote Sensing*, Vol. 57, No. 7, 4322–4331, 2019.
2. Campbell, J. D., A. Melebari, and M. Moghaddam, "Modeling the effects of topography on delay-Doppler maps," *IEEE Journal of Selected Topics in Applied Earth Observations and Remote Sensing*, Vol. 13, 1740–1751, 2020.

3. Unwin, M., P. Jales, J. Tye, C. Gommenginger, G. Foti, and J. Rosello, "Spaceborne GNSS-reflectometry on TechDemoSat-1: Early mission operations and exploitation," *IEEE Journal of Selected Topics in Applied Earth Observations and Remote Sensing*, Vol. 9, No. 10, 4525–4539, 2016.

4. Ruf, C., A. Lyons, M. Unwin, J. Dickinson, R. Rose, D. Rose, and M. Vincent, "CYGNSS: Enabling the future of hurricane prediction [Remote Sensing Satellites]," *IEEE Geoscience and Remote Sensing Magazine*, Vol. 1, No. 2, 52–67, 2013.

5. Clarizia, M. P. and C. S. Ruf, "Wind speed retrieval algorithm for the cyclone global navigation satellite system (CYGNSS) mission," *IEEE Transactions on Geoscience and Remote Sensing*, Vol. 54, No. 8, 4419–4432, 2016.

6. Li, W., E. Cardellach, F. Fabra, A. Rius, S. Ribó, and M. Martín-Neira, "First spaceborne phase altimetry over sea ice using TechDemoSat-1 GNSS-R signals," *Geophysical Research Letters*, Vol. 44, No. 16, 8369–8376, 2017.

7. Nghiem, S. V., C. Zuffada, R. Shah, C. Chew, S. T. Lowe, A. J. Mannucci, E. Cardellach, G. R. Brakenridge, G. Geller, and A. Rosenqvist, "Wetland monitoring with global navigation satellite system reflectometry: Wetland monitoring with GNSS-R," *Earth and Space Science*, Vol. 4, No. 1, 16–39, Hoboken, N.J., 2017.

8. Kim, H. and V. Lakshmi, "Use of cyclone global navigation satellite system (CYGNSS) observations for estimation of soil moisture," *Geophysical Research Letters*, Vol. 45, No. 16, 8272–8282, 2018.

9. Chew, C. C. and E. E. Small, "Soil moisture sensing using spaceborne GNSS reflections: Comparison of CYGNSS reflectivity to SMAP soil moisture," *Geophysical Research Letters*, Vol. 45, No. 9, 4049–4057, 2018.

10. Clarizia, M. P., N. Pierdicca, F. Costantini, and N. Floury, "Analysis of CYGNSS data for soil moisture retrieval," *IEEE Journal of Selected Topics in Applied Earth Observations and Remote Sensing*, Vol. 12, No. 7, 2227–2235, 2019.

11. Shah, R., X. Xu, S. Yueh, C. S. Chae, K. Elder, B. Starr, and Y. Kim, "Remote sensing of snow water equivalent using P-band coherent reflection," *IEEE Geoscience and Remote Sensing Letters*, Vol. 14, No. 3, 309–313, 2017.

12. Tsang, L. and J. A. Kong, *Scattering of Electromagnetic Waves Advanced Topics*, Wiley series in remote sensing, Wiley, 2001.

13. Zavorotny, V. and A. Voronovich, "Scattering of GPS signals from the ocean with wind remote sensing application," *IEEE Transactions on Geoscience and Remote Sensing*, Vol. 38, No. 2, 951–964, 2000.

14. Thompson, D., T. Elfouhaily, and J. Garrison, "An improved geometrical optics model for bistatic GPS scattering from the ocean surface," *IEEE Transactions on Geoscience and Remote Sensing*, Vol. 43, No. 12, 2810–2821, Dec. 2005.

15. Campbell, J. D., et al., "Intercomparison of models for CYGNSS delay-Doppler maps at a validation site in the San Luis Valley of Colorado," *IGARSS 2021*, Brussels, Belgium, Jul. 11–16, 2021.

16. Carreno-Luengo, H., J. A. Crespo, R. Akbar, A. Bringer, A. Warnock, M. Morris, and C. Ruf, "The CYGNSS mission: On-going science team investigations," *Remote Sensing*, Vol. 13, No. 9, 1814, Basel, Switzerland, 2021.

17. Bringer, A., J. Johnson, C. Toth, C. Ruf, and M. Moghaddam, "Studies of terrain surface roughness and its effects on GNSS-R systems using airborne LIDAR measurements," *IGARSS 2021*, Brussels, Belgium, Jul. 11–16, 2021.

18. Dente, L., L. Guerriero, D. Comite, and N. Pierdicca, "Space-borne GNSS-R signal over a complex topography: Modeling and validation," *IEEE Journal of Selected Topics in Applied Earth Observations and Remote Sensing*, Vol. 13, 1218–1233, 2020.

19. Gu, W., H. Xu, and L. Tsang, "A numerical Kirchhoff simulator for GNSS-R land applications," *Progress In Electromagnetics Research*, Vol. 164, 119–133, 2019.

20. Zhu, J., L. Tsang, and H. Xu, "A physical patch model for GNSS-R land applications," *Progress In Electromagnetics Research*, Vol. 165, 93–105, 2019.

21. Xu, H., J. Zhu, L. Tsang, and S. B. Kim, "A fine scale partially coherent patch model including topographical effects for GNSS-R DDM simulations," *Progress In Electromagnetics Research*, Vol. 170, 97–128, 2021.

22. Yueh, S., R. Shah, X. Xu, K. Elder, and B. Starr, "Experimental demonstration of soil moisture remote sensing using P-band satellite signals of opportunity," *IEEE Geoscience and Remote Sensing Letters*, Vol. 17, No. 2, 207–211, 2020.

23. Huang, S., L. Tsang, E. G. Njoku, and K. S. Chan, "Backscattering coefficients, coherent reflectivities, and emissivities of randomly rough soil surfaces at L-band for SMAP applications based on numerical solutions of Maxwell equations in three-dimensional simulations," *IEEE Transactions on Geoscience and Remote Sensing*, Vol. 48, No. 6, 2557–2568, 2010.

24. Al-Khaldi, M. M., J. T. Johnson, S. Gleason, E. Loria, A. J. O'Brien, and Y. Yi, "An algorithm for detecting coherence in cyclone global navigation satellite system mission Level-1 delay-Doppler maps," *IEEE Transactions on Geoscience and Remote Sensing*, Vol. 59, No. 5, 4454–4463, 2021.

25. Jia, Y., S. Jin, H. Chen, Q. Yan, P. Savi, Y. Jin, and Y. Yuan, "Temporal-spatial soil moisture estimation from CYGNSS using machine learning regression with a preclassification approach," *IEEE Journal of Selected Topics in Applied Earth Observations and Remote Sensing*, Vol. 14, 4879–4893, 2021.

26. Munoz-Martin, J. F., L. F. Capon, J. A. Ruiz-de-Azua, and A. Camps, "The flexible microwave Payload-2: A SDR-based GNSS-reflectometer and L-band radiometer for CubeSats," *IEEE Journal of Selected Topics in Applied Earth Observations and Remote Sensing*, Vol. 13, 1298–1311, 2020.

27. Perez-Portero, A., J. F. Munoz-Martin, H. Park, and A. Camps, "Airborne GNSS-R: A key enabling technology for environmental monitoring," *IEEE Journal of Selected Topics in Applied Earth Observations and Remote Sensing*, 1, 2021.

28. Yueh, S. H., R. Shah, X. Xu, B. Stiles, and X. Bosch-Lluis, "A satellite synthetic aperture radar concept using P-band signals of opportunity," *IEEE Journal of Selected Topics in Applied Earth Observations and Remote Sensing*, Vol. 14, 2796–2816, 2021.